Understanding two-pulse phase-modulated decoupling in solid-state NMR

Ingo Scholz,[1] Paul Hodgkinson,[2] Beat H. Meier,[1] and Matthias Ernst[1,a)]
[1]*Physical Chemistry, ETH Zurich, 8093 Zurich, Switzerland*
[2]*Department of Chemistry, Durham University, South Road, Durham DHI 3LE, United Kingdom*

(Received 8 December 2008; accepted 3 February 2009; published online 20 March 2009)

A theoretical description of the two-pulse phase-modulated (TPPM) decoupling sequence in magic-angle spinning NMR is presented using a triple-mode Floquet approach. The description is formulated in the radio-frequency interaction-frame representation and is valid over the entire range of possible parameters leading to the well-known results of continuous-wave (cw) decoupling and XiX decoupling in the limit of a phase change of 0° and 180°, respectively. The treatment results in analytical expressions for the heteronuclear residual coupling terms and the homonuclear spin-diffusion terms. It also allows the characterization of all resonance conditions that can contribute in a constructive or a destructive way to the residual linewidth. Some of the important resonance conditions are described for the first time since they are not accessible in previous treatments. The combination of the contributions from the residual couplings and the resonance conditions to the effective Hamiltonian, as obtained in a Floquet description, is shown to be required to describe the decoupling behavior over the full range of parameters. It is shown that for typical spin system and experimental parameters a ^{13}C linewidth of approximately 12 Hz can be obtained for TPPM decoupling in an organic solid or a protein. This is a major contribution to the experimentally observed linewidths of around 20 Hz and indicates that decoupling techniques are still one of the limiting factors in the achievable linewidths. © *2009 American Institute of Physics*. [DOI: 10.1063/1.3086936]

I. INTRODUCTION

Heteronuclear spin decoupling in the presence of magic-angle sample spinning[1,2] (MAS) is one of the key ingredients to obtain high-resolution spectra in solid-state NMR. With increasing spinning frequencies, the advantages of multiple-pulse decoupling over cw decoupling[3] become more apparent because the residual linewidth under cw decoupling increases with higher spinning frequencies.[4,5] This broadening of the lines is due to the fact that the proton spin diffusion decreases with higher spinning frequencies and the line narrowing due to "self-decoupling"[6,7] is reduced. It is, therefore, essential to use better decoupling schemes at high MAS frequencies.

The first heteronuclear multiple-pulse decoupling sequence that was generally applicable in solids with a dense homonuclear coupling network was the two-pulse phase-modulated (TPPM) decoupling sequence[8] which consists of two pulses with duration τ_p and phase $+\phi$ and $-\phi$, as shown in Fig. 1. The TPPM sequence is widely used for proton decoupling in (bio-)organic solids. While it is easy to implement, the experimental optimization of the sequence requires a two-parameter optimization, namely the pulse length (τ_p) and the phase (ϕ) of the pulses. It is not straightforward to predict the optimum decoupling parameters as a function of the MAS frequency and the rf-field amplitude. In practice, experimental optimization in the two-dimensional parameter space is required.

There are many variants of the TPPM decoupling sequence that were developed in the process of trying to understand and improve the basic sequence: the frequency-modulated and phase-modulated (FMPM) decoupling scheme;[9] the small phase angle rapid cycling (SPARC) sequences;[10] the small phase incremental alternation (SPINAL) sequences;[11] the CPM *m-n* sequences;[12] an amplitude-modulated (AM-TPPM) scheme;[13] the GT-*n* sequences;[14] the continuous-modulation (CM) TPPM sequence;[12,15] and the swept-frequency (SW_f-TPPM) decoupling scheme.[16] The large number of modifications of the original TPPM sequence illustrates the interest in obtaining sequences that are easier to optimize and have a larger range of good decoupling performance. Another approach to the two-parameter optimization problem is the direct spectral optimization of the decoupling sequence on the spectrometer[17] which led to the CM sequence.[15]

There have been other approaches besides the TPPM scheme to the decoupling problem in rotating solids. The symmetry-based rotor-synchronized CN_n^ν sequences can also be used for heteronuclear decoupling. This has been experimentally implemented using hard pulses and the $C12_2^{-1}$ sequence[18] requiring a fixed ratio between the spinning frequency and the rf-field amplitude. A second approach is the use of adiabatic inversion pulses combined with a suitable phase cycle at slower MAS frequencies.[19] Computer optimization of the spin dynamics for model spin systems led to the continuously phase-modulated DROOPY family of decoupling sequences.[20,21] An amplitude-modulated decoupling scheme is the X-inverse-X (XiX) scheme[22,23] which is especially efficient at high MAS frequencies. One can also de-

a)Author to whom correspondence should be addressed. Tel.: +41-44-632-4366. FAX: +41-44-632-1621. Electronic address: maer@ethz.ch.

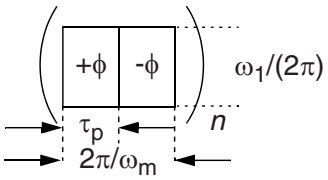

FIG. 1. Schematic representation of the TPPM sequence.

scribe the XiX sequence as a phase-modulated TPPM sequence with a phase $\phi=90°$. It operates, however, in a parameter range where the pulses are considerably longer than in TPPM sequences. At very high spinning frequencies, low-power decoupling schemes become possible[24–27] or the use of rotor-synchronized π pulses in the rotor-synchronized Hahn-echo pulse train experiment.[28]

Analyzing the efficiency of a decoupling method in solid-state NMR under MAS requires the analysis of all terms contributing to the observed linewidth in the spectrum. In general, there are nonresonant and resonant contributions to the effective Hamiltonian. The nonresonant contributions have two parts. (i) The residual second-order coupling terms, which are typically cross terms between the heteronuclear coupling and the chemical-shielding anisotropy (CSA) tensor or a homonuclear coupling. For an ideal decoupling sequence these terms would be zero, but this is not always possible due to the fact that there can be different contributions that cannot be zeroed simultaneously. (ii) Strong homonuclear couplings between the irradiated spins give rise to spin flips or spin diffusion. These spin flips lead to a line narrowing (self-decoupling) of the residual splitting.[6,7] Such a process has very similar characteristics to the line narrowing observed in fast chemical exchange. The resonant contributions can be found at the resonance conditions between the rotation in real space (MAS) and the rotations in spin space (rf irradiation) and can either lead to additional line broadening if heteronuclear couplings are recoupled or to line narrowing if homonuclear dipolar couplings are recoupled and self-decoupling is enhanced.

The quality of heteronuclear decoupling can be measured using either the peak height or the linewidth which is often given as the full width at half height. There is no simple analytical relationship between the two measures of the decoupling quality, but typically the peak height will increase if the linewidth is decreasing. The residual second-order coupling terms will lead to splittings that are manifest as powder line shapes that contain zeroth-rank (isotropic) and fourth-rank contributions. Reducing the residual coupling terms will result in a narrower powder line shape, i.e., a smaller linewidth and also increases the peak intensity. If the overall line shape is unchanged then the peak height will obviously be inversely proportional to the linewidth for these contributions. The effect of the homonuclear couplings on the line shape depends on the relative magnitude of the residual splitting and the rate constant of the spin-flip process. The behavior is similar to that of chemical exchange and can lead to a broadening of the individual multiplet lines or a single line in the center. Averaging over a powder where the residual splittings and the rate constants vary will lead to a complicated line shape where linewidth and peak height are no longer necessarily directly correlated. In this paper, we use the peak height as a criterion because it is experimentally much more easily accessible.

The discussion so far has focused on the observed linewidth or peak height during a free evolution period under decoupling. Another important quantity in the discussion of the performance of heteronuclear decoupling sequences is the refocusable linewidth in spin-echo experiments sometimes called T_2'.[29] In this case, the same contributions to the observed linewidth are present as in the case of the observed linewidth during free evolution. Their impact, however, is different due to the additional refocusing pulse in the spin-echo sequence. In the absence of spin diffusion on the I spins, residual second-order coupling terms will be refocused by the π pulses and do not lead to a decay of the echo intensity. The spin-diffusion process on the I spins, however, cannot be refocused and leads to a decay of the echo intensity if homonuclear and heteronuclear second-order terms are present simultaneously.

A full analysis of decoupling sequences is possible in an interaction frame where the rf Hamiltonian is transformed away. In such an interaction frame, the Hamiltonian is always time dependent with at least two frequencies: the MAS frequency and the basic frequency of the pulse sequence. Depending on the details of the decoupling sequence, additional frequencies can be present in this interaction frame.

Spin systems with multiple time dependencies can be described by average Hamiltonian theory[3,30] (AHT) only by either assuming that the time scales of the two processes are well separated (sequential averaging) or by assuming that they are synchronized and can be characterized by a common single basic frequency. Sequential averaging approaches have been used to describe cw (Ref. 31) and TPPM[20,32] decoupling. The sequential averaging approach can suffer from the limitation that not all resonance conditions can be identified and an incomplete picture of the spin dynamics is obtained. AHT has also been used to describe rotor-synchronized decoupling sequences.[18,33] A better description of time-dependent Hamiltonians with multiple frequencies can be obtained using multimode Floquet theory[34–37] where the case of incommensurate and commensurate frequencies can be treated within a single theoretical framework. Using an operator-based perturbation treatment, one can obtain time-independent effective Hamiltonians. It is then possible to analyze the effective Hamiltonian in terms of the three effects discussed above. Bimodal Floquet theory has been applied to the description of cw[38–40] and XiX decoupling[41] as well as TPPM decoupling.[42]

A detailed analysis of the radio-frequency interaction frame under TPPM irradiation (*vide infra*) shows that in the general case two incommensurate frequencies are needed to describe the interaction-frame transformation. Only in the case of exact π pulses is the interaction-frame transformation described by a single frequency since in this case the TPPM sequence is cyclic, i.e., the propagator of the rf pulses after each TPPM cycle is unity. It is, therefore, best to describe TPPM decoupling using triple-mode Floquet theory[43] where one frequency characterizes the sample spinning and two frequencies the rf interaction-frame transformation. Such an ap-

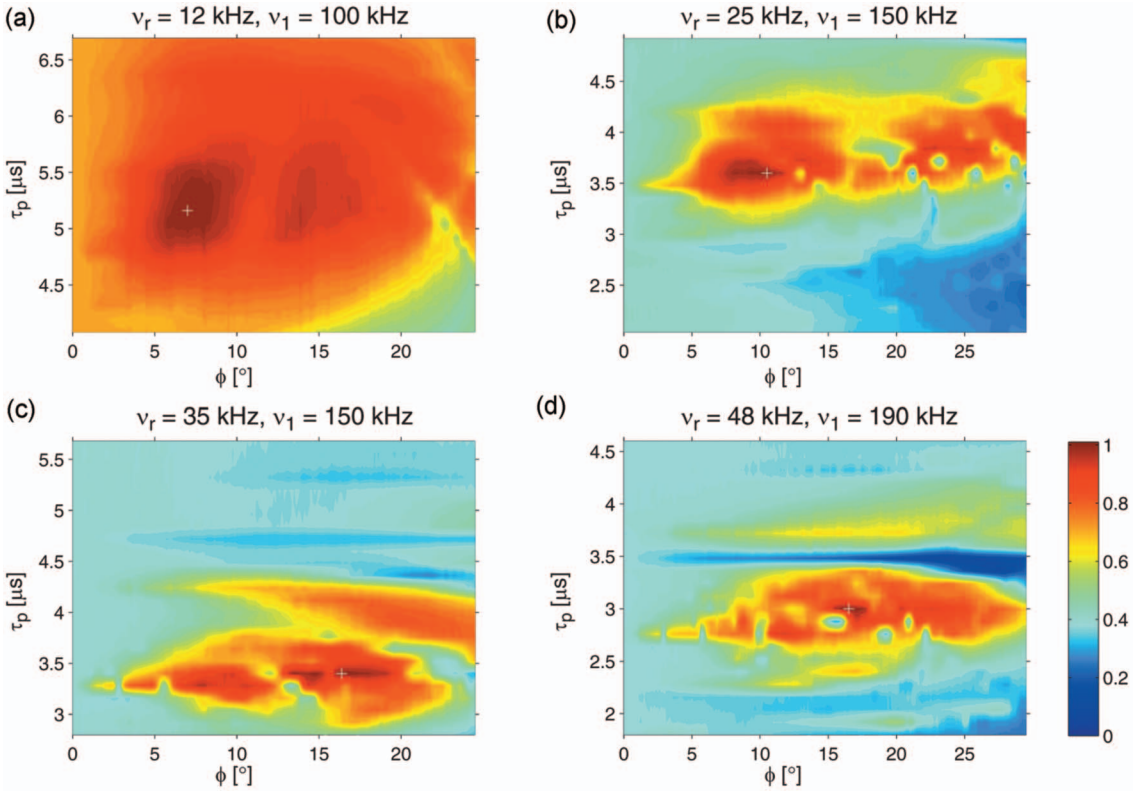

FIG. 2. (Color) Experimental peak height (peak height after Fourier transformation without an apodization function) of the CH_2 group in 1,2-^{13}C-^{15}N-glycine ethylester under TPPM decoupling as a function of the pulse length τ_p and the phase angle ϕ at different experimental conditions: (a) ν_r=12 kHz, ν_1=100 kHz, (b) ν_r=25 kHz, ν_1=150 kHz, (c) ν_r=35 kHz, ν_1=150 kHz, and (d) ν_r=48 kHz, ν_1=190 kHz. The experiments were run on a Varian Infinity+spectrometer with a proton Larmor frequency of 500 MHz using a 1.8 or a 2.5 mm double-resonance MAS probe. The phase resolution of the measurements was 0.25° and the time resolution was 120 ns. The rf-field amplitudes were determined using a proton nutation experiment. The position of the highest intensity is marked by a white +. Numerical values for the parameters at the peak maxima can be found in Table I.

proach allows a unified description of all phenomena observed under TPPM irradiation. The full range of the two parameters τ_p, ϕ can be described without approximations, and the correct results for cw and XiX decoupling are obtained in the limit of ϕ=0° and ϕ=90°. The limitations of the bimodal Floquet treatment[42] where the phase angle has to be small and the pulse length has to be close to the value of a π pulse can be avoided. The full trimodal Floquet description allows the calculation of the nonresonant second-order residual coupling terms, the proton spin-diffusion contribution, as well as all the resonance conditions involving the three different frequencies. These resonance conditions play an important role in the understanding of TPPM decoupling and are described for the first time in detail since they are only partially accessible in previous treatments using AHT[20,32] and bimodal Floquet theory.[42]

In this publication, we first discuss some experimental findings to illustrate the dependence of TPPM decoupling on the MAS frequency and the decoupling rf-field amplitude. In Sec. II, the theoretical basis of TPPM decoupling will be discussed and the effective Hamiltonian for the various relevant situations will be derived. These results will be discussed in the last section and compared to numerical simulations and experimental results.

II. EXPERIMENTAL DATA

Before discussing the details of the theoretical description of TPPM decoupling, some experimental observations are presented, many of which cannot be explained in the framework of the previous theoretical studies of TPPM decoupling.[20,32,42] As discussed above, the line shape under decoupling is determined by the interplay of the residual linewidth due to the second-order cross terms under the decoupling sequence and the influence of the strong coupling network of the abundant spins that can lead to a further line narrowing through self-decoupling.[6,7] Resonance conditions between the three frequencies can lead either to destructive contributions in the form of recoupled heteronuclear couplings or to constructive contributions in the form of recoupled homonuclear dipolar couplings. The contributions to the residual coupling terms and the magnitude and location of the resonance conditions depend on the rf-field amplitude and the spinning frequency in a complex way, leading to a complicated dependence of the parameters with the best decoupling performance on the experimental parameters.

The nonresonant and the resonant effects contribute to the observed peak height and lead to the typical experimental peak-height patterns shown in the plots of Fig. 2. The plots show the peak height of the CH_2 resonance of 1,2-^{13}C-glycine ethylester as a function of the two parameters of the TPPM sequence, the pulse length τ_p and the phase angle ϕ. The position of the maximum peak height is marked by a white "+." At lower MAS frequencies (ν_r =12 kHz (Fig. 2(a)), the area where the peak height is high, corresponding to good decoupling, is quite large. At higher MAS frequencies (ν_r=25 kHz Fig. 2(b); ν_r=35 kHz Fig.

TABLE I. Experimental parameters of Fig. 2.

Figure	ν_1 (kHz)	ν_r (kHz)	$\tau_p^{(\max)}$ (μs)	$\phi^{(\max)}$ (°)	$\tau_p^{(\max)}/\tau_\pi$	$\frac{I(\tau_p^{(\max)},\phi^{(\max)})}{I(\mathrm{cw})}$
2a	100	12	5.2	7.0	1.03	1.4
2b	150	25	3.6	10.5	1.08	2.4
2c	150	35	3.4	16.4	1.02	2.6
2d	190	48	3.0	16.5	1.14	2.5

2(c); ν_r=48 kHz Fig. 2(d)), the range of high peak heights is much narrower, and one can clearly see the influence of resonance conditions where the decoupling performance is bad. For faster spinning, a careful optimization of the parameters is, therefore, essential. Table I summarizes the results of the four experiments of Fig. 2 in terms of the improvement over cw decoupling and the position of the best decoupling in the two-dimensional parameter space spanned by the pulse length τ_p and the phase angle ϕ. While the maximum of the peak height is always close to a pulse length of $\tau_p \approx \tau_\pi$, the position of the optimum phase angle varies over quite a large range between 7° and 17°. The locations of the resonance conditions, leading to "lines" of bad decoupling, change with changing experimental parameters. It is obvious that without understanding the dependence of the location of the resonance conditions on the experimental parameters, a full understanding of the decoupling performance will be impossible.

III. THEORY

Let us consider a spin system which consists of N I and a single S spin. This corresponds to the situation of a rare S spins (e.g., ^{13}C or ^{15}N) coupled to an abundant I spin (e.g., ^{1}H or ^{19}F). In a tilted coordinate system where the I-spin coordinate system was rotated by 90° about the y axis, such that the quantization axis of the I spins is aligned along the axis of the static part of the rf field irradiation, the tilted rotating-frame Hamiltonian is given by

$$\begin{aligned}\mathcal{H}(t) = &\sum_{n=-2}^{2} \omega_S^{(n)} e^{in\omega_r t} S_z - \sum_{\ell=1}^{N}\sum_{n=-2}^{2} \omega_{I_\ell}^{(n)} e^{in\omega_r t} I_{\ell x} \\ &- \sum_{\ell=1}^{N}\sum_{n=-2}^{2} \omega_{SI_\ell}^{(n)} e^{in\omega_r t} 2S_z I_{\ell x} \\ &+ \sum_{\ell<m}\sum_{\substack{n=-2 \\ n\neq 0}}^{2} \omega_{I_\ell I_m}^{(n)} e^{in\omega_r t}[3I_{\ell x}I_{mx} - (\vec{I_\ell}\cdot\vec{I_m})] \\ &+ \sum_{\ell<m} \omega_{I_\ell I_m}^{(0)} (\vec{I_\ell}\cdot\vec{I_m}) + \omega_1 \sum_{\ell=1}^{N} (I_{\ell z}\cos(\varphi(t)) \\ &+ I_{\ell y}\sin(\varphi(t))), \end{aligned} \tag{1}$$

where the rf-field part of the Hamiltonian was written as a general phase-modulated irradiation. The Fourier coefficients of the various interactions of Eq. (1) are given in Appendix A. In TPPM decoupling, the phase modulation has the form of a square wave which can be described by

$$\phi(t) = \frac{4\phi_0}{\pi}\sum_{k=1}^{\infty}\frac{1}{2k-1}\sin((2k-1)\omega_m t). \tag{2}$$

In CM decoupling[15] the Fourier series consists only of the k=1 term. Note that the maximum value for the phase of the first Fourier component is by a factor of $4/\pi$ larger than the value of the phase of the square wave. This will become important for the experimental comparison of the square-wave (TPPM) and CM decoupling sequences (*vide infra*). For TPPM decoupling, it is assumed that the phases are given by $\pm\phi$ and the pulse length is given by τ_p leading to a modulation frequency of $\omega_m = \pi/\tau_p$.

By going into an interaction frame with the radio-frequency part of the Hamiltonian, the system Hamiltonian acquires additional time dependencies and Eq. (1) can be rewritten in a general way as

$$\begin{aligned}\tilde{\mathcal{H}}(t) = &\sum_{n=-2}^{2} \omega_S^{(n)} e^{in\omega_r t} S_z - \sum_{\ell=1}^{N}\sum_{n=-2}^{2} \omega_{I_\ell}^{(n)} e^{in\omega_r t} \tilde{I}_{\ell x} \\ &- \sum_{\ell=1}^{N}\sum_{n=-2}^{2} \omega_{SI_\ell}^{(n)} e^{in\omega_r t} 2S_z \tilde{I}_{\ell x} \\ &+ \sum_{\ell<m}\sum_{\substack{n=-2 \\ n\neq 0}}^{2} \omega_{I_\ell I_m}^{(n)} e^{in\omega_r t}[3\tilde{I}_{\ell x}\tilde{I}_{mx} - (\vec{I_\ell}\cdot\vec{I_m})] \\ &+ \sum_{\ell<m} \omega_{I_\ell I_m}^{(0)} (\vec{I_\ell}\cdot\vec{I_m}), \end{aligned} \tag{3}$$

where the tilde indicates that operators are in the interaction frame. The spin operators in the interaction frame can always be represented as a linear combination of the three Cartesian spin operators in the laboratory frame with time-dependent coefficients,

$$\begin{aligned}\tilde{I}_x(t) &= a_{xx}(t)I_x + a_{xy}(t)I_y + a_{xz}(t)I_z, \\ \tilde{I}_y(t) &= a_{yx}(t)I_x + a_{yy}(t)I_y + a_{yz}(t)I_z, \\ \tilde{I}_z(t) &= a_{zx}(t)I_x + a_{zy}(t)I_y + a_{zz}(t)I_z. \end{aligned} \tag{4}$$

The time-dependent coefficients $a_{\nu\mu}(t)$ can be expressed as Fourier series with multiple basic frequencies. For TPPM decoupling two incommensurate frequencies have to be included, namely, the basic modulation frequency of the pulse sequence

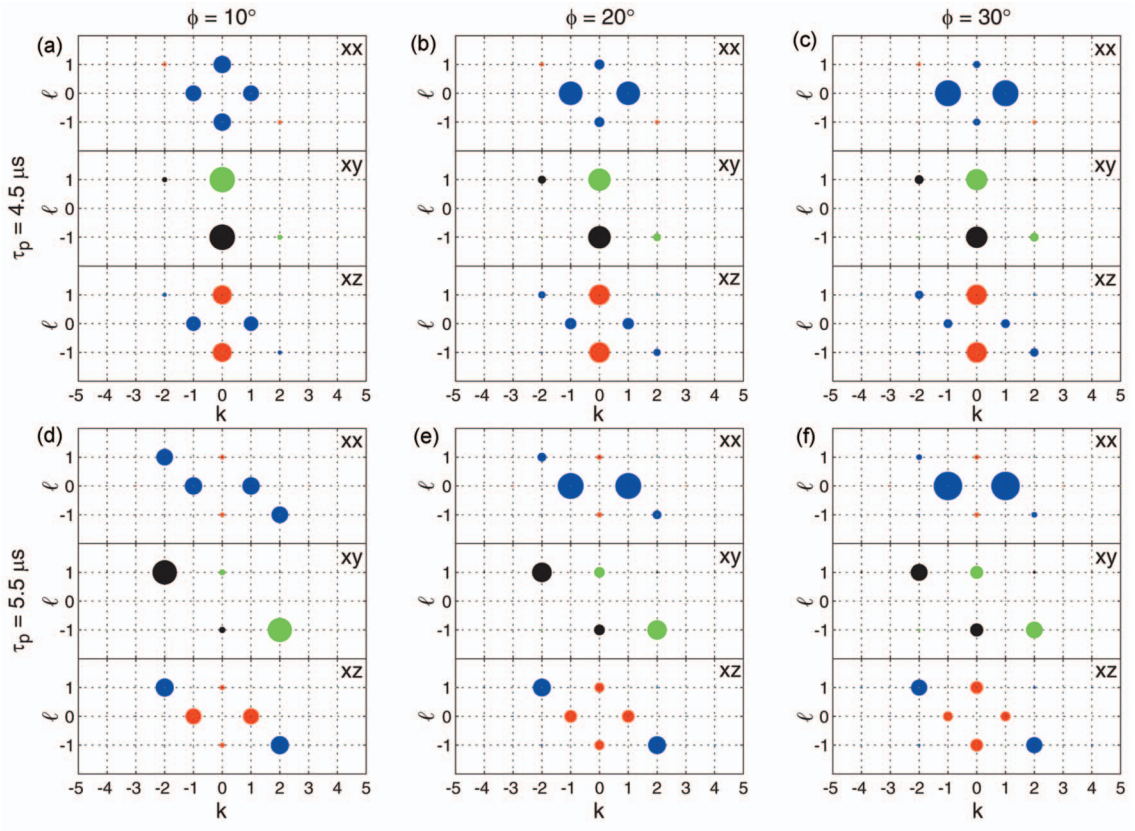

FIG. 3. (Color) Plot of the complex phase and the magnitude of the Fourier coefficients $\alpha_{x\mu}^{(k,\ell)}$ for $\mu=x$, y, and z for a rf field amplitude of $\nu_1=100$ kHz for two different pulse lengths $\tau_p=4.5$ μs ((a)–(c)) and 5.5 μs ((d)–(f)) and three different phase angles $\phi=10°$ ((a) and (d)), 20° ((b) and (e)), and 30° ((c) and (f)). The diameter of the circles indicates the magnitude and the color the sign and complex phase of the Fourier coefficients. Blue indicates that the Fourier coefficient is positive and real, red that it is negative and real, black that it is positive and imaginary, and green that it is negative and imaginary.

$$\omega_m = \frac{\pi}{\tau_p} \tag{5}$$

and an additional frequency

$$\omega_\alpha = \frac{\alpha}{\pi}\omega_m, \tag{6}$$

where

$$\alpha = \arccos(\cos\beta\cos^2\phi + \sin^2\phi). \tag{7}$$

Here, β is the flip angle of one of the pulses given by

$$\beta = \pi\frac{\omega_1}{\omega_m}. \tag{8}$$

The frequency ω_α corresponds to the magnitude of the effective nutation about an axis which describes the combined rotation of the two pulses in a TPPM cycle. An expression for ω_α can be obtained by an analytical calculation of the time evolution of the spin system over complete cycles of the TPPM sequence. This is given in Appendix B. The time-dependent coefficients can be written as a Fourier series with the two frequencies as

$$a_{\nu\mu}(t) = \sum_{k=-\infty}^{\infty}\sum_{\ell=-\infty}^{\infty} a_{\nu\mu}^{(k,\ell)} e^{ik\omega_m t} e^{i\ell\omega_\alpha t}. \tag{9}$$

A closer inspection of the possible Fourier coefficients shows that the index ℓ is limited to the range $(-1,0,1)$ (see Appendix). The Fourier coefficients $a_{\nu\mu}^{(k,\ell)}$ have been calculated by a numerical integration of an interaction-frame trajectory. For the homonuclear two-spin terms in Eq. (3), it is helpful to introduce a simplified notation for the Fourier coefficients and define

$$a_{xx,\nu\mu}^{(k,\ell)} = \sum_{k_1=-\infty}^{\infty}\sum_{\ell_1=-1}^{1} a_{x\nu}^{(k_1,\ell_1)} a_{x\mu}^{(k-k_1,\ell-\ell_1)}. \tag{10}$$

Note that the index ℓ for the two-spin coefficients spans the range of $-2,\ldots,2$. The index k goes from $-\infty$ to ∞. However, for the range of pulse lengths considered here ($\tau_p \leqslant \tau_{2\pi}$ or $\omega_m > \omega_1/2$), numerical calculations show that the Fourier coefficients $|k|>2$ are small and can be neglected without significant changes in the results.

Figure 3 shows a plot of the Fourier coefficients $a_{x\mu}^{(k,\ell)}$ for $\mu=x$, y, and z for a rf field amplitude of $\nu_1=100$ kHz two different pulse length $\tau_p=4.5$ and 5.5 μs and three different phase angles $\phi=10°$, 20°, and 30°. The diameter of the circles indicates the magnitude and the color the sign and complex phase of the Fourier coefficients. There are some general properties that are fulfilled for the Fourier coefficients,

$$a_{x\mu}^{(k,\ell)} = (a_{x\mu}^{(-k,-\ell)})^*. \tag{11}$$

The Fourier coefficients $a_{xx}^{(k,\ell)}$ and $a_{xz}^{(k,\ell)}$ are always real while $a_{xy}^{(k,\ell)}$ is always imaginary. These properties will become im-

portant later to discuss the properties of the effective Hamiltonians.

The complete time-dependent interaction-frame Hamiltonian can be written as a function of three frequencies as

$$\tilde{\mathcal{H}}(t) = \sum_{n=-2}^{2} \sum_{k=-\infty}^{\infty} \sum_{\ell=-2}^{2} \tilde{\mathcal{H}}^{(n,k,\ell)} e^{in\omega_r t} e^{ik\omega_m t} e^{i\ell\omega_\alpha t}, \tag{12}$$

with the Fourier coefficients of the Hamiltonian $\tilde{\mathcal{H}}^{(n,k,\ell)}$ given by

$$\begin{aligned}
\tilde{\mathcal{H}}^{(0,0,0)} &= \omega_S^{(0)} S_z + \sum_{p<m} \omega_{I_p I_m}^{(0)} \vec{I}_p \cdot \vec{I}_m - \sum_p (\omega_{I_p}^{(0)} + \omega_{SI_p}^{(0)} 2S_z) \\
&\quad \times (a_{xx}^{(0,0)} I_{px} + a_{xy}^{(0,0)} I_{py} + a_{xz}^{(0,0)} I_{pz}), \\
\tilde{\mathcal{H}}^{(n,0,0)} &= \omega_S^{(n)} S_z - \sum_p (\omega_{I_p}^{(n)} + \omega_{SI_p}^{(n)} 2S_z)(a_{xx}^{(0,0)} I_{px} + a_{xy}^{(0,0)} I_{py} \\
&\quad + a_{xz}^{(0,0)} I_{pz}) + \sum_{p<m} \omega_{I_p I_m}^{(n)} \Bigg[3 \sum_{\nu,\mu} a_{xx,\nu\mu}^{(0,0)} I_{p\nu} I_{m\mu} \\
&\quad - (\vec{I}_p \cdot \vec{I}_m) \Bigg], \\
\tilde{\mathcal{H}}^{(n,k,\ell)} &= - \sum_p (\omega_{I_p}^{(0)} + \omega_{SI_p}^{(0)} 2S_z)(a_{xx}^{(k,\ell)} I_{px} + a_{xy}^{(k,\ell)} I_{py} \\
&\quad + a_{xz}^{(k,\ell)} I_{pz}) + \Bigg(\sum_{p<m} 3\omega_{I_p I_m}^{(n)} \sum_{\nu,\mu} a_{xx,\nu\mu}^{(k,\ell)} I_{p\nu} I_{m\mu} \Bigg) \\
&\quad \times (1 - \delta_{n,0}),
\end{aligned} \tag{13}$$

where $\delta_{n,0}$ is the Kronecker delta function. Note that the index ℓ is limited to $|\ell| \leqslant 1$ for one-spin operators and to $|\ell| \leqslant 2$ for two-spin operators. The problem can now be treated with a standard triple-mode Floquet description.[43] The effective Hamiltonian for such a triple-mode Floquet problem is given by

$$\bar{\mathcal{H}} = \sum_{n_0,k_0,\ell_0} \tilde{\mathcal{H}}^{(n_0,k_0,\ell_0)} + \sum_{n_0,k_0,\ell_0} \tilde{\mathcal{H}}_{(2)}^{(n_0,k_0,\ell_0)} + \cdots, \tag{14}$$

with

$$\tilde{\mathcal{H}}_{(2)}^{(n_0,k_0,\ell_0)} = -\frac{1}{2} \sum_{\nu,\kappa,\gamma} \frac{[\tilde{\mathcal{H}}^{(n_0-\nu,k_0-\kappa,\ell_0-\lambda)}, \tilde{\mathcal{H}}^{(\nu,\kappa,\lambda)}]}{\nu\omega_r + \kappa\omega_m + \lambda\omega_p}. \tag{15}$$

Note the summation conventions used here, n_0, k_0, and ℓ_0, will only sum over the values for which the condition $n_0\omega_r + k_0\omega_m + \ell_0\omega_\alpha = 0$ is fulfilled, while ν, κ, and λ will only sum over the values for which the condition $\nu\omega_r + \kappa\omega_m + \lambda\omega_\alpha \neq 0$ is fulfilled. The calculation of the interaction-frame transformations, the Fourier coefficients, and the effective Hamiltonians was done using the software package MATHEMATICA (Wolfram Research Inc., Champaign, IL).

As discussed in Sec. I the line shape observed in the spectrum can be correlated with the contributions to the effective Hamiltonian. There are two different types of contributions to the effective Hamiltonian: (i) nonresonant contributions that show up in the different orders of $\tilde{\mathcal{H}}_{(p)}^{(0,0,0)}$ and (ii) resonant contributions that show up in the different orders of $\tilde{\mathcal{H}}_{(p)}^{(n_0,k_0,\ell_0)}$ if the resonance condition $n_0\omega_r + k_0\omega_m + \ell_0\omega_\alpha = 0$ is fulfilled. The residual line broadening under TPPM irradiation is given by the heteronuclear terms in the nonresonant part of the effective Hamiltonian,

$$\bar{\mathcal{H}} = \tilde{\mathcal{H}}^{(0,0,0)} + \tilde{\mathcal{H}}_{(2)}^{(0,0,0)} + \cdots, \tag{16}$$

while the homonuclear I-spin couplings are given by the homonuclear terms of Eq. (16). In order to make the discussion clearer, the nonresonant effective Hamiltonian will be divided into three parts,

$$\bar{\mathcal{H}} = \bar{\mathcal{H}}_{IS} + \bar{\mathcal{H}}_{IIS} + \bar{\mathcal{H}}_{II}, \tag{17}$$

which will be discussed separately. The first part contains the heteronuclear terms originating from cross terms between the heteronuclear coupling and the I-spin CSA tensor, the second one heteronuclear terms originating from the cross terms between heteronuclear and homonuclear couplings, and the third one the purely homonuclear I-spin terms. The effective Hamiltonians at the resonance conditions are given by the resonant first-order and second-order contributions to the effective Hamiltonian,

$$\begin{aligned}
\bar{\mathcal{H}} &= \sum_{n_0,k_0,\ell_0} \tilde{\mathcal{H}}^{(n_0,k_0,\ell_0)} + \tilde{\mathcal{H}}^{(-n_0,-k_0,-\ell_0)} + \sum_{n_0,k_0,\ell_0} \tilde{\mathcal{H}}_{(2)}^{(n_0,k_0,\ell_0)} \\
&\quad + \tilde{\mathcal{H}}_{(2)}^{(-n_0,-k_0,-\ell_0)} + \ldots.
\end{aligned} \tag{18}$$

Analytical results for these terms are given here and the implications will be discussed in Sec. IV.

The heteronuclear terms of the nonresonant part of the effective Hamiltonian, i.e., terms containing mixed I-spin and S-spin spin operators, consist of zeroth-order contributions from the heteronuclear J coupling and second-order cross terms between the heteronuclear coupling and the I-spin chemical-shift anisotropy,

$$\begin{aligned}
\bar{\mathcal{H}}_{IS} &= \omega_S^{(0)} S_z - 2S_z \sum_p \omega_{I_p S}^{(0)} (a_{xx}^{(0,0)} I_{px} + a_{xy}^{(0,0)} I_{py} + a_{xz}^{(0,0)} I_{pz}) \\
&\quad + iS_z \sum_p \sum_{\nu=-2}^{2} (q_{xx}^{(\nu)} I_{px} + q_{xy}^{(\nu)} I_{py} + q_{xz}^{(\nu)} I_{pz})(\omega_{I_p S}^{(-\nu)} \omega_{I_p}^{(\nu)} \\
&\quad + \omega_{I_p S}^{(\nu)} \omega_{I_p}^{(-\nu)}).
\end{aligned} \tag{19}$$

The analytical expressions for the constants $q_{x\mu}^{(\nu)}$ can be found in Appendix C. The second-order cross terms between heteronuclear and homonuclear dipolar couplings are given by

$$\begin{aligned}
\bar{\mathcal{H}}_{IIS} &= -\frac{3}{4} i \sum_{p<m} \sum_{\nu=-2}^{2} \Bigg[(\omega_{I_m S}^{(-\nu)} \omega_{I_p I_m}^{(\nu)} - \omega_{I_m S}^{(\nu)} \omega_{I_p I_m}^{(-\nu)}) \\
&\quad \times \sum_{\mu,\chi} q_{z\mu\chi}^{(\nu)} 4S_z I_{p\mu} I_{m\chi} + (\omega_{I_p S}^{(-\nu)} \omega_{I_p I_m}^{(\nu)} - \omega_{I_p S}^{(\nu)} \omega_{I_p I_m}^{(-\nu)}) \\
&\quad \times \sum_{\mu,\chi} \tilde{q}_{z\mu\chi}^{(\nu)} 4S_z I_{p\mu} I_{m\chi} \Bigg].
\end{aligned} \tag{20}$$

The constants $q_{z\mu\chi}^{(\nu)}$ and $\tilde{q}_{z\mu\chi}^{(\nu)}$ are defined in Appendix C. The terms of Eqs. (19) and (20) describe residual heteronuclear couplings in the effective Hamiltonian that are manifest in the spectrum as a residual splitting of the resonance line under TPPM decoupling.

The homonuclear I-spin terms in the nonresonant part of the effective Hamiltonian contains one-spin fictitious-field terms and multispin coupling terms,

$$\begin{aligned}\bar{\mathcal{H}}_{II} = & \sum_{p<m} \omega^{(0)}_{I_pI_m} \vec{I}_p \cdot \vec{I}_m - \sum_p \omega^{(0)}_{I_p} (a^{(0,0)}_{xx} I_{px} + a^{(0,0)}_{xy} I_{py} \\ & + a^{(0,0)}_{xz} I_{pz}) + \frac{i}{2} \sum_p \sum_{\nu=-2}^{2} (q^{(\nu)}_{xx} I_{px} + q^{(\nu)}_{xy} I_{py} + q^{(\nu)}_{xz} I_{pz}) \\ & \times (\omega^{(-\nu)}_{I_p} \omega^{(\nu)}_{I_p} + \omega^{(-\nu)}_{I_pS} \omega^{(\nu)}_{I_pS}) \\ & - \frac{9}{8} i \sum_{p,\ell<m} \sum_{\nu=-2}^{2} \omega^{(\nu)}_{I_\ell I_m} \omega^{(-\nu)}_{I_\ell I_m} \sum_\mu p^{(\nu)}_\mu I_{\ell\mu} \\ & - \frac{9}{2} i \sum_{\ell<m<o} \sum_{\nu=-2}^{2} (\omega^{(\nu)}_{I_\ell I_m} \omega^{(-\nu)}_{I_m I_o} \\ & - \omega^{(-\nu)}_{I_\ell I_m} \omega^{(\nu)}_{I_m I_o}) \sum_{\mu,\chi,\xi} p^{(\nu)}_{\mu\chi\xi} I_{\ell\mu} I_{m\chi} I_{o\xi}. \end{aligned} \tag{21}$$

The fictitious-field terms lead to a small shift of the second-order resonance conditions, i.e., the contributions by the $\tilde{\mathcal{H}}^{(n_0,k_0,\ell_0)}_{(2)}$ terms, while the homonuclear coupling terms are responsible for the spin-diffusion process that manifests itself as self-decoupling and a line narrowing in the spectrum. A definition of the coefficients $p^{(\nu)}_{\mu\chi\xi}$, $p^{(\nu)}_\mu$ is given in Appendix C.

The zeroth-order contributions to the effective Hamiltonian on the resonance conditions are given by

$$\bar{\mathcal{H}} = \tilde{\mathcal{H}}^{(n_0,k_0,\ell_0)} + \tilde{\mathcal{H}}^{(-n_0,-k_0,-\ell_0)}, \tag{22}$$

with

$$\begin{aligned}\tilde{\mathcal{H}}^{(n_0,k_0,\ell_0)} = & -(\omega^{(n_0)}_{I_\ell} + 2\omega^{(n_0)}_{I_\ell S} S_z)(a^{(k_0,\ell_0)}_{xx} I_{\ell x} + a^{(k_0,\ell_0)}_{xy} I_{\ell y} \\ & + a^{(k_0,\ell_0)}_{xz} I_{\ell z}) + \left(\sum_{p<m} 3\omega^{(n_0)}_{I_pI_m} \sum_{\nu,\mu} a^{(k_0,\ell_0)}_{xx,\nu\mu} I_{p\nu} I_{m\mu} \right) \\ & \times (1 - \delta_{n_0,0}), \end{aligned} \tag{23}$$

and contain homonuclear and heteronuclear terms. Therefore, these resonance conditions can lead to a broadening of the line if the heteronuclear contributions are important. If the heteronuclear contributions are small and the homonuclear terms large, such resonance conditions can lead to an increasing spin-diffusion process resulting in a line narrowing due to self-decoupling.

The second-order contributions to the effective Hamiltonian on the resonance conditions are given by

$$\bar{\mathcal{H}} = \tilde{\mathcal{H}}^{(n_0,k_0,\ell_0)}_{(2)} + \tilde{\mathcal{H}}^{(-n_0,-k_0,-\ell_0)}_{(2)}, \tag{24}$$

with

$$\begin{aligned}\tilde{\mathcal{H}}^{(n_0,k_0,\ell_0)}_{(2)} = & \frac{i}{2} \sum_p \sum_{\nu=-2}^{2} (q^{(\nu,k_0,\ell_0)}_{xx} I_{px} + q^{(\nu,k_0,\ell_0)}_{xy} I_{py} + q^{(\nu,k_0,\ell_0)}_{xz} I_{pz}) \times (\omega^{(n_0-\nu)}_{I_p} \omega^{(\nu)}_{I_p} + \omega^{(n_0-\nu)}_{I_pS} \omega^{(\nu)}_{I_pS} + 2(\omega^{(n_0-\nu)}_{I_pS} \omega^{(\nu)}_{I_p} + \omega^{(\nu)}_{I_pS} \omega^{(n_0-\nu)}_{I_p}) S_z) \\ & - \frac{3}{4} i \sum_{p<m} \sum_{\nu=-2}^{2} [(\omega^{(n_0-\nu)}_{I_mS} \omega^{(\nu)}_{I_pI_m} - \omega^{(\nu)}_{I_mS} \omega^{(n_0-\nu)}_{I_pI_m}) \sum_{\mu,\chi} q^{(\nu,k_0,\ell_0)}_{z\mu\chi} 4 S_z I_{p\mu} I_{m\chi} + (\omega^{(n_0-\nu)}_{I_pS} \omega^{(\nu)}_{I_pI_m} \\ & - \omega^{(\nu)}_{I_pS} \omega^{(n_0-\nu)}_{I_pI_m}) \sum_{\mu,\chi} \bar{q}^{(\nu,k_0,\ell_0)}_{z\mu\chi} 4 S_z I_{p\mu} I_{m\chi}] + \frac{i}{2} \sum_p \sum_{\nu=-2}^{2} (q^{(\nu,k_0,\ell_0)}_{xx} I_{px} + q^{(\nu,k_0,\ell_0)}_{xy} I_{py} + q^{(\nu,k_0,\ell_0)}_{xz} I_{pz}) (\omega^{(n_0-\nu)}_{I_p} \omega^{(\nu)}_{I_p} + \omega^{(n_0-\nu)}_{I_pS} \omega^{(\nu)}_{I_pS}) \\ & - \frac{9}{8} i \sum_{p,\ell<m} \sum_{\nu=-2}^{2} \omega^{(\nu)}_{I_\ell I_m} \omega^{(n_0-\nu)}_{I_\ell I_m} \sum_\mu p^{(\nu,k_0,\ell_0)}_\mu I_{\ell\mu} - \frac{9}{2} i \sum_{\ell<m<o} \sum_{\nu=-2}^{2} (\omega^{(\nu)}_{I_\ell I_m} \omega^{(n_0-\nu)}_{I_m I_o} - \omega^{(n_0-\nu)}_{I_\ell I_m} \omega^{(\nu)}_{I_m I_o}) \sum_{\mu,\chi,\xi} p^{(\nu,k_0,\ell_0)}_{\mu\chi\xi} I_{\ell\mu} I_{m\chi} I_{o\xi}. \end{aligned} \tag{25}$$

The corresponding terms can be expressed in full analogy to the effective Hamiltonians for the nonresonant case (see Eqs. (19)–(21) and Appendix), taking into account the additional general summation restrictions for the resonant case.

In the limiting case of cw decoupling ($\phi=0$), the characteristic frequencies reduce to $\omega_\alpha=\omega_1$ while ω_m becomes meaningless. It follows that the relevant Fourier coefficients are restricted to corresponding pairs $(0,\ell)$ with $\ell=-2,\ldots,2$. In the case of XiX decoupling ($\phi=\pi/2$), ω_α vanishes and ω_m remains as defined in Eq. (5). In this case, only Fourier coefficients corresponding to pairs $(k,0)$ with $k=-\infty,\ldots,\infty$ are relevant. Thus in both cases, our theoretical framework is reduced to a bimodal Floquet approach.[38,41] In the case of π pulses, one finds $\omega_m=\omega_1$, $\alpha=2\phi$, and, therefore, $\omega_\alpha=(2\phi/\pi)\omega_m$. For the case of ϕ being a rational multiple of π, the interaction frame can always be characterized by a single frequency and a collapse of the triple-mode Floquet description into a bimodal Floquet description is possible.

The theoretical description of TPPM decoupling using effective Hamiltonians based on triple-mode Floquet theory uses an interaction-frame representation where the rf part of the Hamiltonian is transformed away. In principle, such an interaction-frame transformation requires that stroboscopic observations with multiples of the cycle time of the interaction-frame transformation are used. In the case of heteronuclear decoupling, however, the observation is done on

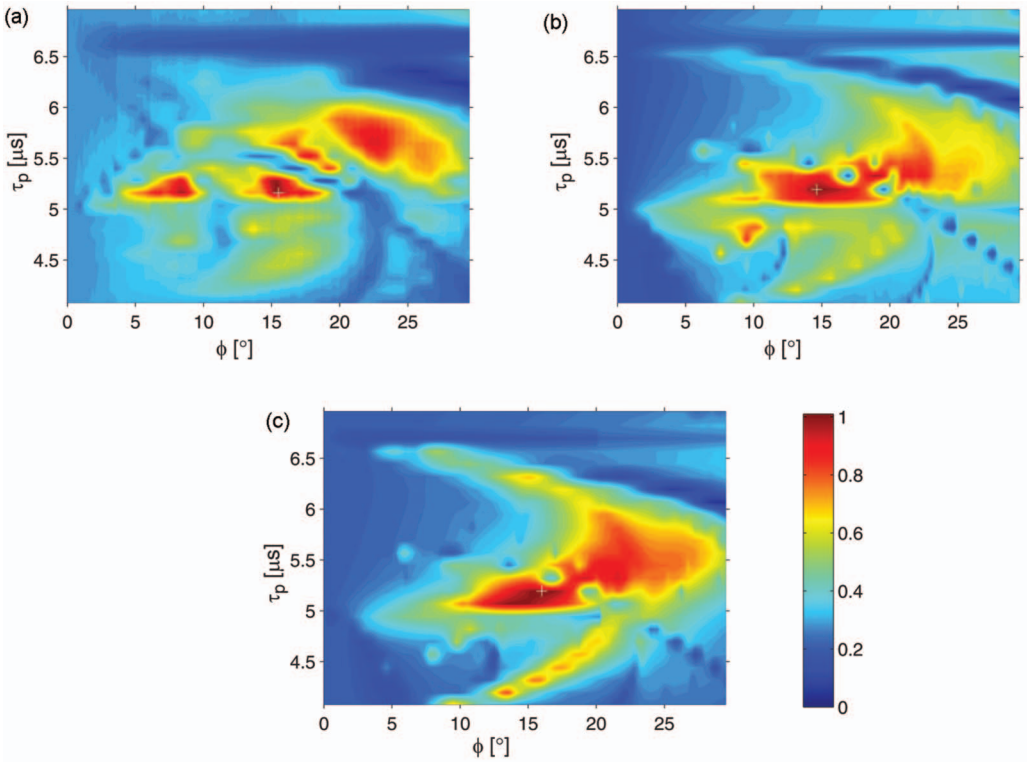

FIG. 4. (Color) (a) Experimental peak height (peak height after Fourier transformation without apodization) of the CH_2 group in 1,2-^{13}C-^{15}N-glycine ethylester under TPPM decoupling as a function of the pulse length τ_p and the phase angle ϕ at ν_r=25 kHz and ν_1=100 kHz. The experiments were run on a Varian Infinity+spectrometer with a proton Larmor frequency of 500 MHz using a 2.5 mm double-resonance MAS probe. The phase resolution of the measurements was 0.25° and the time resolution was 120 ns. The rf-field amplitude was determined using a proton nutation experiment. Numerical simulations of the peak height as a function of the pulse length τ_p and the phase angle ϕ using (b) a five-spin CH_4 system and (c) three-spin CH_2-type spin system. The simulations were carried out using the PNMRSIM simulation package. The spinning frequency in all simulations was set to ν_r=25 kHz and the rf amplitude was set to ν_1=100 kHz. The phase resolution of the simulation was 0.25° and the time resolution was 125 ns. All dipolar couplings were included in the simulations as well as isotropic and anisotropic chemical shifts. The peak height was simulated for a powder average of 1000 crystallite orientations.

the *S* spins which are in the usual rotating frame. Therefore, no stroboscopic observation is required in our case.

IV. RESULTS AND DISCUSSION

In addition to the analysis of the effective Hamiltonians based on Floquet theory, numerical simulations are used to characterize the features of TPPM decoupling. Experimental conditions of ν_r=25 kHz and ν_1=100 kHz will be used throughout this section to discuss and illustrate the features of TPPM decoupling where numerical calculations are required. The *I*-spin CSA tensor was always assumed to be axially symmetric and have an anisotropy of 3 kHz. All simulations were carried out using the PNMRSIM package[44] which is optimized for efficiently simulating large spin systems including specific optimization for calculating the time evolution under phase-modulated decoupling sequences.[45] To assess the size of the proton spin system that is required to obtain realistic simulations, experimental data were compared to numerical simulations with a variable number of proton spins. Figure 4 shows a comparison of experimental data (Fig. 4(a)) i.e., the peak height of the CH_2 group in glycine ethylester under TPPM decoupling as a function of the pulse length and the phase angle at a MAS frequency of 25 kHz and a rf-field amplitude of 100 kHz. The numerical simulations using a five-spin (CH_4) system (Fig. 4(b)) and a three-spin (CH_2) system (Fig. 4(c)) show that already relatively small spin systems can reproduce the experimental observations of Fig. 1 quite well. One can clearly see the same type of resonance conditions in the experimental and the simulated data. Note that the simulations do not include any rf-field inhomogeneities, while the experimental data of Fig. 2 were measured with a probe of which the rf-field inhomogeneity was determined by a nutation experiment to be 10 kHz (full width at half height) over the nutation profile. Including rf-field inhomogeneities into the numerical simulations would be straightforward but is computationally expensive. Since we do not expect any significant changes in the features except a smoothing of the resonances, inhomogeneity was neglected in all simulations. From the results in Fig. 4, we conclude that the general features of TPPM decoupling are already visible in three-spin systems and further numerical simulations described here were calculated for three-spin systems.

To estimate the importance of the various interactions, numerical simulations of TPPM decoupling in a three-spin CH_2 system have been carried out where selected interactions have been left out. Figure 5(a) shows the simulated peak height at a MAS spinning frequency of 25 kHz and a rf-field amplitude of 100 kHz where all interactions (CSA, homonuclear, and heteronuclear dipolar couplings, for details, see the figure caption) have been taken into account. Figure 5(b) shows the same simulations without the

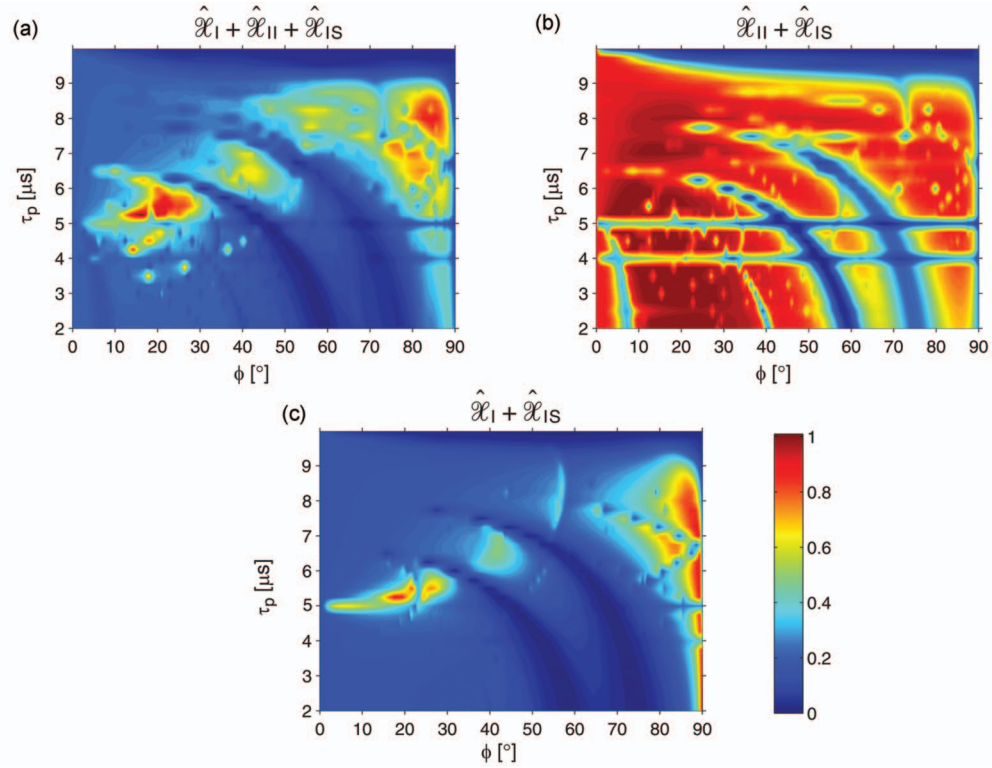

FIG. 5. (Color) Numerical simulations of the peak height as a function of the pulse length τ_p and the phase angle ϕ using a three-spin CH_2 system as used in Fig. 4(b) but with an extended range of parameters. (a) Full simulation including all interactions. (b) Simulation without the proton chemical-shift tensor. (c) Simulation without the proton homonuclear dipolar coupling. Otherwise, in all simulations the same parameters were used as for the simulation shown in Fig. 4(b), except that the phase resolution of the simulation was 0.5° and the time resolution was 250 ns.

chemical-shift tensors of the protons, while in Fig. 5(c) the homonuclear dipolar coupling was set to zero. It is obvious that the proton CSA tensor is the main reason for the low peak intensity (i.e., broad lines) in large areas of the parameter space which confirms that a second-order cross term between the heteronuclear dipolar coupling and the proton CSA tensors ($\bar{\mathcal{H}}_{(a)}$) is the dominating term for the residual line with in cw and TPPM decoupling.[31,38] The homonuclear dipolar coupling becomes important at $\phi=90°$ which corresponds to XiX decoupling and confirms that for amplitude-modulated decoupling sequences the second-order cross term between the homonuclear and the heteronuclear dipolar coupling is the dominating term for the residual linewidth.[41] One can also clearly see that the area of good decoupling (high peak height) around $\tau_p=5.2$ μs and $\phi=20°$ is significantly reduced illustrating the beneficial influence of the homonuclear dipolar coupling on the peak height. There are strong resonance conditions visible which degrade the decoupling quality and will be classified and discussed in detail in the following.

Based on the effective Hamiltonians calculated in Sec. III, the nonresonant and resonant contributions determining the residual linewidth under heteronuclear decoupling will now be analyzed. The nonresonant residual coupling terms under TPPM decoupling are given by Eq. (19) ($\bar{\mathcal{H}}_{IS}$: cross terms between heteronuclear couplings and the I-spin chemical shifts) and Eq. (20) ($\bar{\mathcal{H}}_{IIS}$: cross terms between heteronuclear and homonuclear dipolar couplings). These terms are the source of the residual line splitting under the decoupling sequence.

The zeroth-order contributions in the Hamiltonian $\bar{\mathcal{H}}_{IS}$ of Eq. (19) are cross terms between the isotropic chemical shifts and J couplings (known as off-resonance decoupling[46,47] under cw irradiation) and will not be discussed further due to the small magnitude of the J couplings compared to the dipolar couplings. The magnitude of the second-order terms is determined by the constants $q_{x\mu}^{(\nu)}=q_{x\mu}^{(\nu,0,0)}$ (see Appendix, Eqs. (C1)–(C3)). Perfect decoupling (no residual linewidth) would be achieved for $\bar{\mathcal{H}}_{IS}=0$ which depends on the relative orientation of the two tensors. In practice, good decoupling will be achieved in areas where all the coefficients $q_{x\mu}^{(\nu)}$ are small compared to the Fourier coefficients of the interactions (see Eq. (19)).

From the symmetry properties of the Fourier coefficients $a_{x\mu}^{(k,\ell)}$ (Eq. (11)), it follows that $q_{xy}^{(\nu)}=0$. Figure 6 shows contour plots of the four $q_{x\mu}^{(\nu)}$ coefficients for $\mu=x,z$ and $|\nu|=1,2$ (red: negative contours; blue: positive contours) superimposed on a grayscale density plot of the full numerical simulation of Fig. 5(a). One can clearly see that the area of best decoupling corresponds with the area where all the coefficients $q_{x\mu}^{(\nu)}$ are small (where the color changes from red to blue), i.e., small angles ϕ and pulse lengths in the order of the length of a π pulse. The detailed shape of this area will depend on the relative orientation of the two tensors, but one can expect good decoupling for pulse length slightly longer than a π pulse and for phase angles between 5° and 30°. If one adds up the absolute values of all four terms shown in Fig. 6, the minimum of the second-order cross terms lies on the line $\tau_p=\tau_\pi/\cos\phi$. As expected, the $q_{zx}^{(\nu)}$ terms are zero for

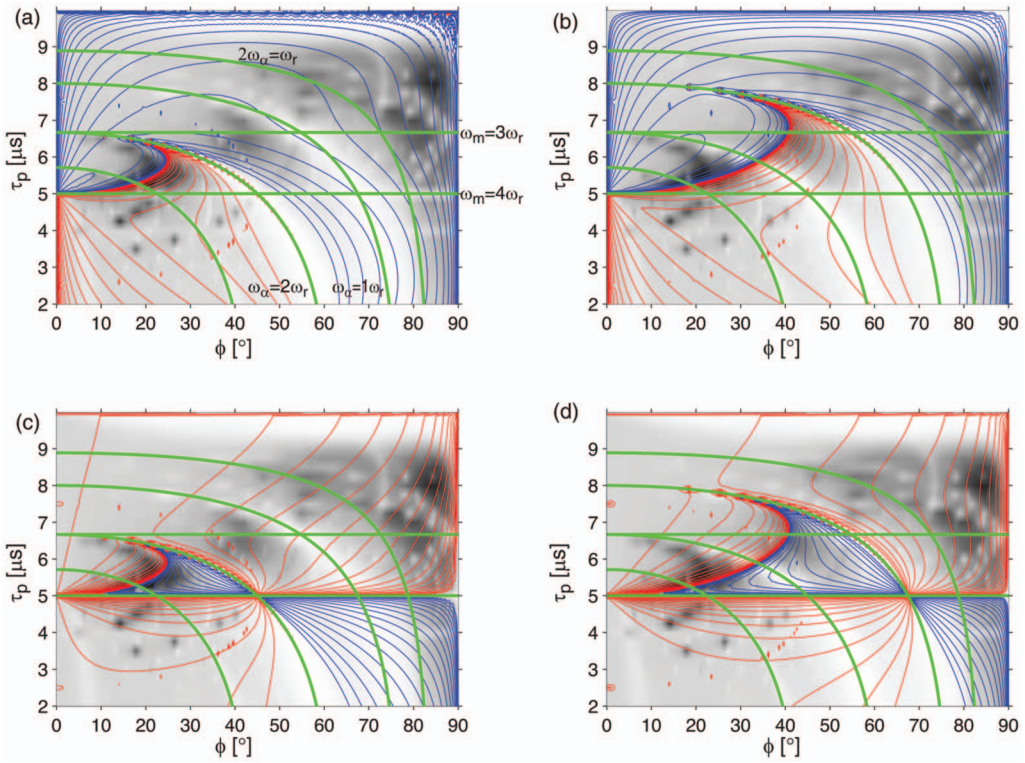

FIG. 6. (Color) Contour plots (blue and red lines) of the coefficients $q_{x\mu}^{(\nu)}$ for (a) $\mu=x$, $\nu=\pm1$; (b) $\mu=z$, $\nu=\pm1$; (c) $\mu=x$, $\nu=\pm2$; and (d) $\mu=z$, $\nu=\pm2$. These contour plots are superimposed on a grayscale density plot of the numerical simulations of a CH_2 spin system shown in Fig. 5(a). In addition, the resonance conditions $\omega_m=n_0\omega_r$ (straight lines) and $\omega_\alpha=n_0\omega_r$ (curved lines) are shown using green lines.

cw decoupling ($\phi=0$), while the $q_{zz}^{(\nu)}$ terms are nonvanishing.[38] For XiX decoupling ($\phi=90°$), all $q_{z\mu}^{(\nu)}$ terms become zero and the residual linewidth is no longer determined by the cross terms between the heteronuclear dipolar coupling and the *I*-spin CSA tensors.[41] The heteronuclear cross terms become large (and decoupling bad) close to zeroth-order resonance conditions (green lines in Fig. 6) where the heteronuclear dipolar coupling is recoupled (*vide infra*).

For the Hamiltonian $\bar{\mathcal{H}}_{IIS}$ of Eq. (20) there are only second-order contributions from cross terms between the heteronuclear and homonuclear dipolar couplings. These terms are small compared to the contributions by $\bar{\mathcal{H}}_{IS}$ except for $\phi=90°$ (XiX decoupling) and close to some resonance conditions which will be discussed later. A contour plot (blue contours) of the sum of all 18 coefficients, $\Sigma_{\mu,\chi}|q_{z\mu\chi}^{(\nu)}|+\Sigma_{\mu,\chi}|\tilde{q}_{z\mu\chi}^{(\nu)}|$, is shown in Fig. 7(a) for $\nu=\pm1$ and in Fig. 7(c) for $\nu=\pm2$. Due to smallness of these terms, they will not contribute significantly to the residual splitting, except in XiX decoupling. In the case of XiX decoupling, they are the leading terms for the residual splitting due to the fact that the ISxI terms are averaged out.[41] The green lines indicate again the location of some selected resonance conditions.

The purely *I*-spin homonuclear contribution to the nonresonant part of the second-order Hamiltonian is given by $\bar{\mathcal{H}}_{II}$ [Eq. (21)]. The zeroth-order part contains the homonuclear *J* couplings and the isotropic chemical-shift terms of the *I* spins, while the second-order part contains fictitious-field terms that lead to small shift of the resonance conditions. The main contributions, however, are the second-order three-spin homonuclear dipolar cross terms that promote spin diffusion on the *I* spins. These homonuclear terms play a role mainly in areas where the residual linewidth is already small. These terms are significant over the whole range of parameters, as can be seen from the contour plot (blue lines) of the sum of the coefficients, $\Sigma_{\mu,\chi,\xi}|p_{\mu x\xi}^{(\nu)}|$, in Fig. 7(b) for $\nu=\pm1$ and in Fig. 7(d) for $\nu=\pm2$. One can also see that the terms become very large close to zeroth-order resonance conditions (green lines in Fig. 7) where the homonuclear dipolar coupling is recoupled (*vide infra*). These second-order terms are not present in the numerical simulations shown in Fig. 5 due to the limited size of the spin system.

From the discussion of the nonresonant terms in the second-order effective Hamiltonian, it is clear that the area of good decoupling (narrow line, high peak intensity) is determined by the cross terms between the *I*-spin CSA tensors and the heteronuclear dipolar couplings. In a second step, the possible resonance conditions that can show up under TPPM decoupling have to be analyzed. There are different types of resonance conditions $n_0\omega_r+k_0\omega_m+\ell_0\omega_\alpha=0$ that play an important role in understanding the decoupling performance. They can show up as zeroth-order resonance conditions where the generalized effective Hamiltonian is given by Eqs. (22) and (23) or as second-order resonance condition where the effective Hamiltonian is given by Eqs. (24) and (25). A complete description of the potential resonance conditions is only possible in the full radio-frequency interaction frame used here which requires a triple-mode Floquet treatment.

The first class of resonance conditions is found for $n_0\omega_r+k_0\omega_m=0$ which shows up as horizontal lines in the

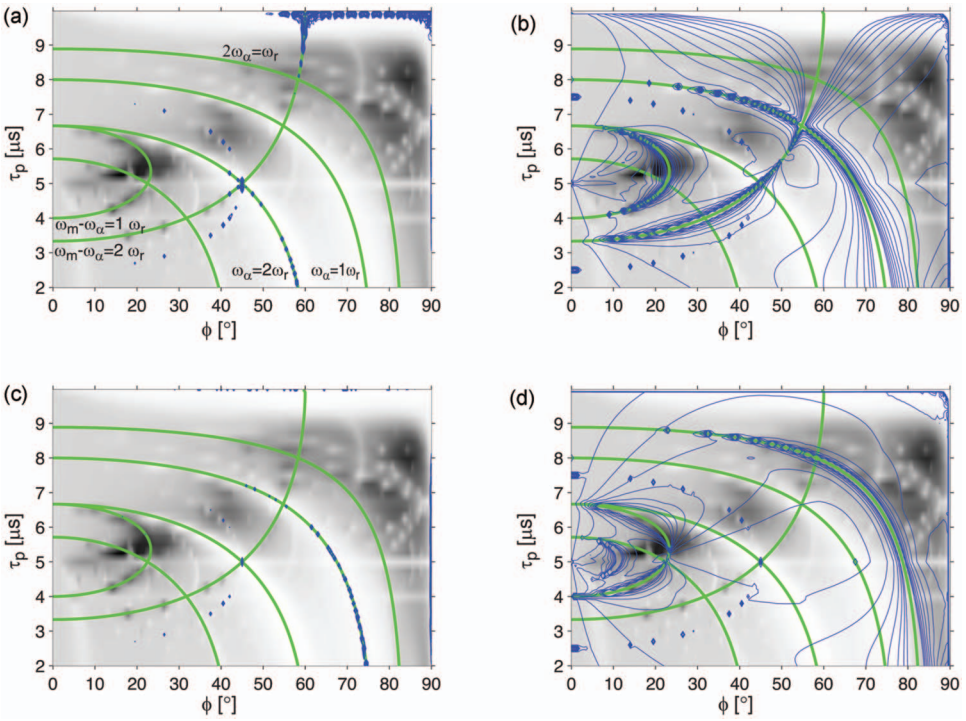

FIG. 7. (Color) Contour plot of the sum of the heteronuclear coefficients $\Sigma_{\mu,\chi}|q^{(\nu)}_{z\mu\chi}|+\Sigma_{\mu,\chi}|\tilde{q}^{(\nu)}_{z\mu\chi}|$ for (a) $\nu=\pm1$ and (c) $\nu=\pm2$ and the sum of the homonuclear coefficients $\Sigma_{\mu,\chi,\xi}|p^{(\nu)}_{\mu x\xi}|$ for (b) $\nu=\pm1$ and (d) $\nu=\pm2$. These plots are superimposed on a grayscale density plot of the numerical simulations of a CH_2 spin system shown in Fig. 5(a). In addition, the resonance conditions $2\omega_\alpha-\omega_m=n_0\omega_r$ and $\ell_0\omega_\alpha=n_0\omega_r$ are shown using green lines.

two-dimensional TPPM decoupling plots (Fig. 8(a)). They correspond to a recoupling of the heteronuclear (and homonuclear) dipolar coupling in zeroth order for $n_0=\pm1$ and ±2, $k_0=1$, and $\ell_0=0$ and in second order for $n_0=\pm3$ and ±4. Even third-order recoupling conditions of the heteronuclear dipolar coupling are visible for $n_0=\pm5$ and ±6. The zeroth-order resonance conditions lie outside the plotted area at $\tau_p=10$ and 20 μs, respectively. In zeroth order, the

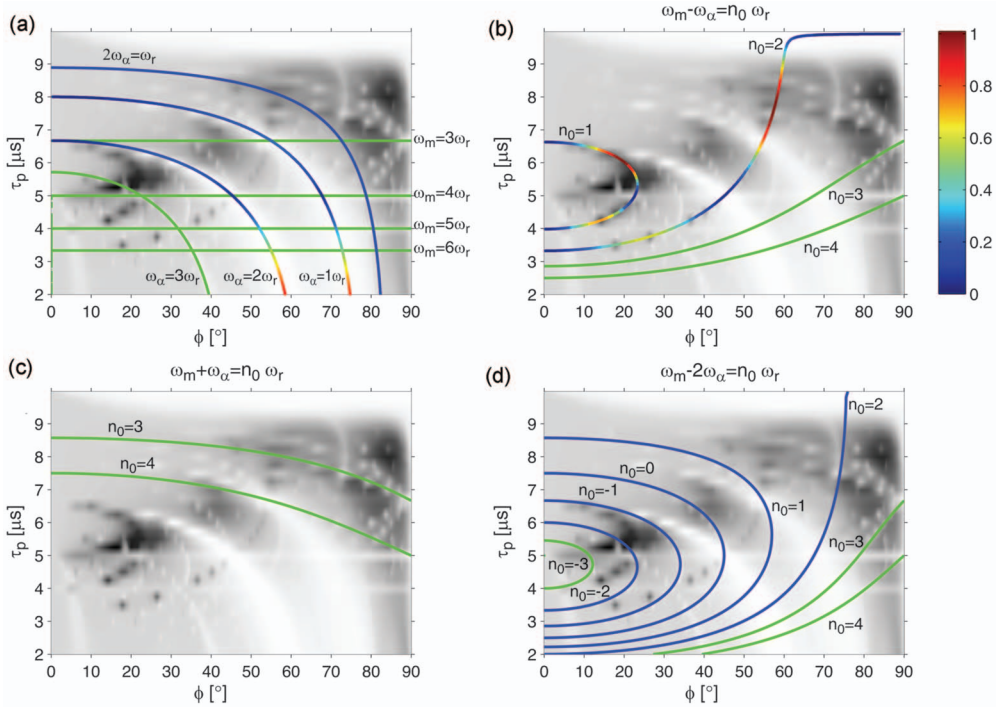

FIG. 8. (Color) Plots of the resonance conditions encountered in TPPM decoupling. The location of the resonance conditions (n_0,k_0,ℓ_0) are plotted as lines (blue or color coded: zeroth-order resonance conditions: green: second-order or third-order resonance conditions) superimposed on a grayscale density plot of the numerical simulations of a CH_2 spin system shown in Fig. 5(a). (a) Straight lines correspond to the resonance conditions $(n_0,1,0)$ which recouple heteronuclear dipolar couplings; curved lines correspond to resonance conditions $(n_0,0,1)$ which also recouple heteronuclear dipolar coupling. The strength of the resonance condition is given by the magnitude of the $a^{(1,0)}_{x\mu}$ and $a^{(0,1)}_{x\mu}$ Fourier coefficient, respectively. The magnitude of some of the zeroth-order resonance conditions has been color coded on the lines. (b) $(n_0,\pm1,\mp1)$ resonance conditions which result in zeroth order ($n_0=1$ and 2) in a purely homonuclear dipolar Hamiltonian. Again, the magnitude of the resonance terms has been color coded on the line. (c) $(n_0,\pm1,\pm1)$ resonance condition. (d) $(n_0,\pm1,\pm2)$ resonance condition.

strength of the heteronuclear recoupling condition is determined by the magnitude of the $a_{x\mu}^{(1,0)}$ Fourier coefficients. For the second-order terms, the sum over the products of the coefficients as shown in Eq. (25) gives the strength of the resonance condition. At these resonance conditions, the homonuclear dipolar coupling and the CSA tensors of the protons are also recoupled, but their influence on the *S*-spin spectrum is not as strong.

The second class of resonance conditions is given by $n_0\omega_r+\ell_0\omega_\alpha=0$ and show up in Fig. 8(a) as curved lines. They correspond to a recoupling of the heteronuclear dipolar coupling in zeroth order for $n_0=\pm1$ and ±2, $k_0=0$, and $\ell_0=1$ and 2 and in second order for $n_0=\pm3$ and ±4. The strength of the zeroth-order recoupling is given by the Fourier coefficients $a_{x\mu}^{(0,1)}$ for the heteronuclear terms and by $a_{xx,\mu\nu}^{(0,1)}$ and $a_{xx,\mu\nu}^{(0,2)}$ for the homonuclear terms. The strength of the heteronuclear terms is color coded on the contour lines for the $n_0=1$ and 2 resonance conditions. One can clearly see that the strength of the heteronuclear contribution to the resonance condition increases with increasing phase angle, which is also reflected in the numerical simulations. Although CSA tensors and homonuclear dipolar couplings are also recoupled, their influence on the *S*-spin spectrum is not as strong. The zeroth-order $n_0=1$, $\ell_0=2$ resonance condition is a purely homonuclear resonance condition due to the fact that the $a_{x\mu}^{(0,2)}$ coefficients are zero. For the second-order recoupling conditions the sums of products of Eq. (25) have to be considered. In second order, cross terms between the heteronuclear dipolar coupling and the *I*-spin CSA tensors or the homonuclear dipolar coupling are the source of the broadening. The zeroth-order recoupling conditions are also visible in the plots of the nonresonant heteronuclear terms and homonuclear terms (Figs. 6 and 7). For the $\ell_0=1$, $n_0=\pm1$ and ±2 conditions, the cross terms between the CSA tensor and the heteronuclear dipolar couplings are quite small in the vicinity of the resonance condition for small angles ϕ, but for larger angles ϕ they increase dramatically (Fig. 6). For the $\ell_0=1$, $n_0=\pm1$ and the $\ell_0=2$, $n_0=\pm1$ conditions, we also find a strong homonuclear contribution, as can be seen from Figs. 7(b) and 7(d).

A third class of resonance conditions involves all three frequencies and is characterized by $n_0\omega_r+k_0\omega_m+\ell_0\omega_\alpha=0$. The first example in this class, $n_0\omega_r\pm\omega_m\mp\omega_\alpha=0$, is plotted in Fig. 8(b). Since the $a_{x\mu}^{(\pm1,\mp1)}$ Fourier coefficients are always zero, no recoupling of the heteronuclear dipolar couplings happens in zeroth order, and purely homonuclear terms are obtained due to the fact that the $a_{xx,\mu\nu}^{(\pm1,\mp1)}$ terms are nonzero. This corresponds to a "HORROR-type" recoupling condition, which can be used in homonuclear polarization-transfer experiments,[48] where the recoupling sequence decouples the decoupling at the same time. Such a recoupling is beneficial in the context of decoupling since it leads to additional line narrowing if the residual coupling is sufficiently small. The magnitude of the $a_{xx,\mu\nu}^{(\pm1,\mp1)}$ Fourier coefficients is color coded in the contour lines and one can see a strong variation in the magnitude as a function of the TPPM parameters. The maximum of the $n_0=1$ and 2 resonance conditions is in the area where good decoupling is achieved. The same can also be seen from the homonuclear nonresonant homonuclear terms shown in Figs. 7(b) and 7(d). The homonuclear dipolar cross terms are very strong around the zeroth-order $n_0=1$ and 2 resonance conditions, while the heteronuclear cross terms (Figs. 6 and 7) show no such behavior.

The resonance conditions $n_0\omega_r\pm\omega_m\pm\omega_\alpha=0$ are shown in Fig. 8(c). The zeroth-order conditions for $n_0=1$ and 2 are outside the plotted area and only the weak second-order resonance conditions for $n_0=3$ and 4 are shown. They have homonuclear and heteronuclear contributions and do not give rise to strong features in the plots of the decoupling efficiency. The recoupling condition $n_0\omega_r\pm\omega_m\mp2\omega_\alpha=0$ is shown in Fig. 8(d). The zeroth-order contributions (blue lines) for this resonance condition are purely homonuclear since the $a_{x\mu}^{(k,2)}$ Fourier coefficients are all zero. In second order (green lines), homonuclear and heteronuclear cross terms can contribute to the effective Hamiltonian.

The results discussed so far are combined in Fig. 9 which shows the same four experimental data sets already shown in Fig. 2. In addition, the theoretical location of the minima of the residual coupling terms (second-order cross terms between CSA tensor and heteronuclear dipolar coupling) has been marked by a dotted white line ($\tau_p=\tau_\pi/\cos\phi$). One can clearly see that the points of maximum peak height are in all cases close to the theoretical line. In addition, some of the resonance conditions have also been included as white (purely homonuclear) and black (homonuclear and heteronuclear) lines. Again, one can clearly see that the resonance conditions explain most of the areas of low peak height. Differences in the location between the theoretical resonance lines and the experimental measurements could originate from errors in calibrating the rf-field amplitude or from the presence of rf-field inhomogeneities. A more detailed prediction of the location of the maximum peak height as a function of the spinning frequency and the rf-field amplitude is difficult. A change in ω_r will only change the location of the resonance conditions, while a change in ω_1 will change the location of the resonance conditions as well as the position of the location of the minimum for the second-order residual coupling terms.

For small values of ω_r and large values of ω_1, the area of good decoupling is relatively large due to the fact that most of the destructive resonance conditions fall outside the area of good decoupling. For faster spinning, the destructive resonance conditions move into the area of good decoupling and make a precise optimization of the parameters important. To find the parameters for the best decoupling performance, a two-dimensional optimization of the TPPM parameters within the limits of 5° and 20° for the phase and between τ_π and $1.2\tau_\pi$ for the pulse length should always give the optimum results. As a rule of thumb for finding the optimum TPPM decoupling condition, the following strategy seems to be the most efficient. For a pulse length which is slightly longer than a π pulse, the phase is optimized between 5° and 20°. At the point with the best decoupling, the time is now optimized in a second step while keeping the phase fixed. This second optimization can be limited to roughly $\pm10\%$ of the pulse length but the steps should be fairly small.

The actual linewidth (full width at half height) of the

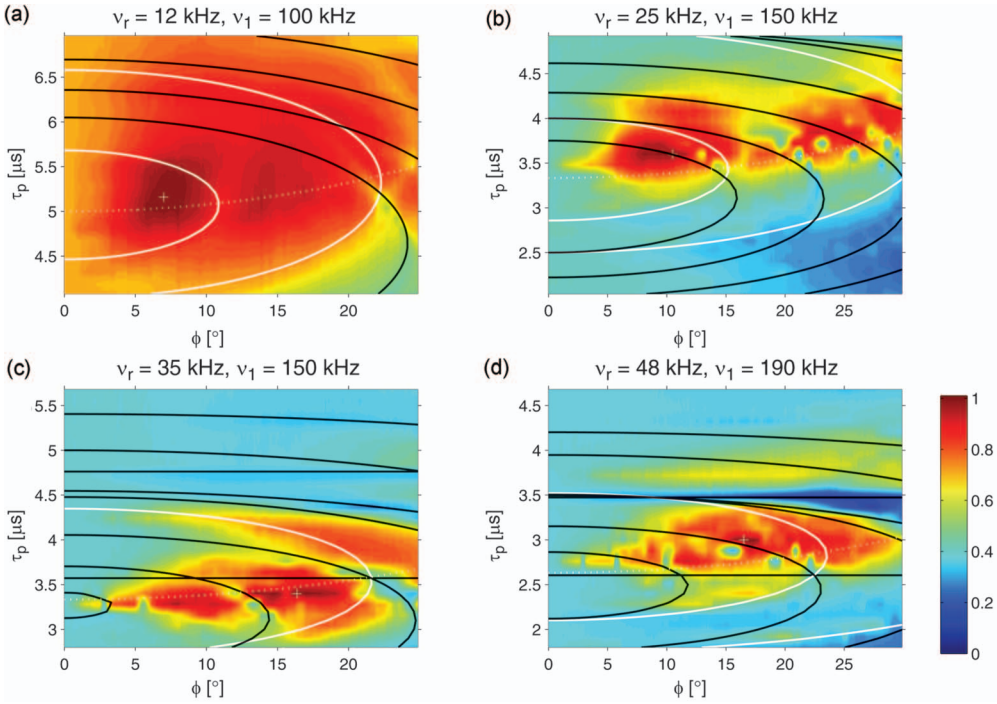

FIG. 9. (Color) Contour plots of the decoupling efficiency shown in Fig. 2 ((a) ν_r=12 kHz, ν_1=100 kHz, (b) ν_r=25 kHz, ν_1=150 kHz, (c) ν_r=35 kHz, ν_1=150 kHz, and (d) ν_r=48 kHz, ν_1=190 kHz) with the location of the theoretical minimum of the second-order cross terms plotted as a white dotted line. The resonance conditions are shown as white lines for purely homonuclear resonance conditions and as black line for heteronuclear and homonuclear resonance conditions.

simulated data of Fig. 5(a) ranges from 12 Hz to more than 10 kHz. In the area of the maximum peak height corresponding to the minimum linewidth, the linewidth depends very strongly on the pulse length. A change of 0.20 μs in the pulse length leads to a linewidth of more than 50 Hz. The combination of rf-field inhomogeneities with such a strong dependence of the linewidth on the pulse length can explain the observed experimental linewidths in the range of 20–30 Hz.

Besides the inhomogeneous linewidth during a free evolution period (T_2), the homogeneous linewidth corresponding to the decay of the echo intensity under a spin-echo sequence (determined by T_2') is also an important quantity in solid-state NMR experiments. Figure 10 shows a comparison between the peak height as a function of the TPPM decoupling parameters during a free evolution period (Fig. 10(a)) and the intensity of the spin echo (Fig. 10(b)), using a fixed echo time of τ=10 ms. This signal intensity is used as a measure for T_2'. One can clearly see that for the spin-echo experiment, the areas of high peak height (corresponding to long T_2' times) are much smaller and limited to the area where the heteronuclear cross terms are small. This can be understood from the properties of the spin-echo sequence which refocuses the heteronuclear second-order terms but not the homonuclear I-spin second-order contributions. Strong echoes can only be obtained in areas where either the heteronuclear or the homonuclear second-order contributions are small. If both contributions are present, the echo will be weak due to a simultaneous evolution under the heteronuclear and homonuclear terms which cannot be refocused.

In the original TPPM decoupling sequence[8] a square-wave implementation of the phase modulation was used while in the CM decoupling sequence[12,15] the phase modulation is implemented by a continuous sine modulation. Such a sequence is a special case of the more general CPM m-n sequences.[12] The Fourier series describing the square-wave phase modulation contains a sum of sine terms (see Eq. (2)). In the corresponding CM implementation only the lowest Fourier coefficient of the full series is used. Figure 10 shows a comparison of the peak height of the CH_2 group in 1,2-^{13}C-glycine ethylester under TPPM (Fig. 10(a)) and CM (Fig. 10(c)) decoupling. The performance of TPPM and CM decoupling is almost indistinguishable in the observed range of the two parameters τ_p and ϕ if one takes into account a scaling of the maximum phase by a factor of $4/\pi$ as one would expect from the Fourier expansion of a square wave (see Eq. (2)). The same observation is also true for the use of TPPM or CM decoupling in spin-echo sequences to measure the T_2' decay times. Again one finds that the two sequences give virtually identical results (Figs. 10(b) and 10(d)). This result can be understood from the full interaction frame discussed in Sec. III. In the range of typical TPPM parameters ($\tau_p \leqslant \tau_{2\pi}$ or $\omega_m > \omega_1/2$ and $\phi < 40°$), the interaction frame of the continuous phase-modulated CM decoupling scheme has the same two frequencies as TPPM decoupling. The Fourier coefficients are also only significant for $|\ell| \leqslant 1$ and $|k| \leqslant 2$ and almost identical to the Fourier coefficients found for the square-wave TPPM irradiation. This explains why the TPPM and CM decoupling schemes show an almost identical behavior which was already shown experimentally in the publication about the CPM sequences.[12]

Low-power TPPM and XiX decoupling can also be analyzed in the framework of the general description presented here. Due to the fact that the pulse length is much longer

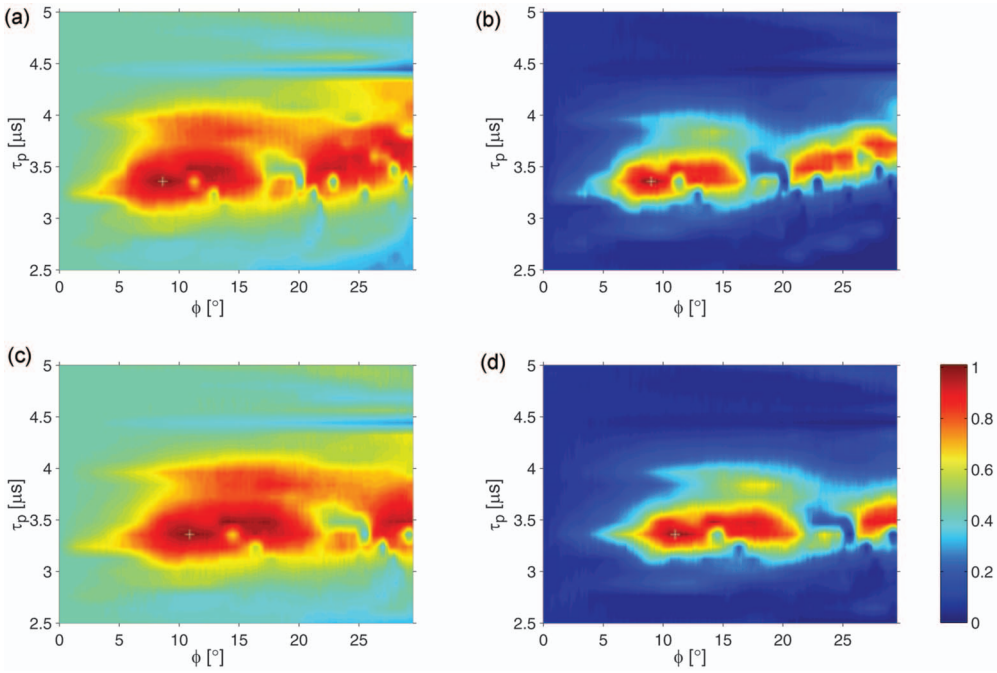

FIG. 10. (Color) Comparison of TPPM and CM decoupling for direct observation [(a) and (c)] and the spin-echo ($T_{2'}$) experiment [(b) and (d)]. The plots show the experimental peak height (peak height after Fourier transformation without an apodization function) of the CH_2 group in 1,2-^{13}C-^{15}N-glycine ethylester under TPPM or CM decoupling as a function of the pulse length τ_p and the phase angle ϕ at a spinning frequency of 28 kHz and a rf-field amplitude of 158 kHz: (a) peak height under TPPM decoupling ($I(3.36\ \mu s, 8.6°)=9.3\times10^6$), (c) peak height under CM decoupling ($I(3.36\ \mu s, 10.9°)=9.2\times10^6$), (b) peak height after a spin-echo sequence ($T_{2'}$) with $\tau=10$ ms and TPPM decoupling ($I(3.36\ \mu s, 9.0°)=4.4\times10^6$), (d) peak height after a spin-echo sequence ($T_{2'}$) with $\tau=10$ ms and CM decoupling ($I(3.36\ \mu s, 11.0°)=4.3\times10^6$). The experiments were run on a Varian Infinity+ spectrometer with a proton Larmor frequency of 500 MHz using a 2.5 mm double-resonance MAS probe. The phase resolution of the measurements was 0.25° and the time resolution was 120 ns. The rf-field amplitudes were determined using a proton nutation experiment. The position of the highest intensity is marked by a white +.

and, therefore, the modulation frequency of the pulse sequence much lower, different considerations come into play. We plan to investigate and characterize them in detail in the future.

V. CONCLUSIONS

In this work, a general description of TPPM decoupling under MAS in solid-state NMR has been presented. The description is based on a trimodal Floquet formalism. The analysis shows that for all phase angles except close to or at 90°, the cross term between the CSA tensor and the heteronuclear dipolar coupling dominates the residual coupling. Only near $\phi=90°$ does, the cross term between the heteronuclear and the homonuclear dipolar coupling becomes important, as is known from the analysis of XiX decoupling. The residual couplings are never zero due to contributions from different Fourier components that depend differently on the external parameters. The residual couplings, i.e., the CSA dipolar-coupling cross terms, have a minimum along the line $\tau_p=\tau_\pi/\cos\phi$, and we expect the area of good decoupling close to this line for phase angles ϕ smaller than 20°. The homonuclear dipolar cross terms are quite large over the whole range of parameters, with extreme values along purely homonuclear resonance conditions. The detailed location of the optimum TPPM parameters depends on the position of the resonance conditions, which change with spinning frequency and rf-field amplitude. The full set of potential resonance conditions have been described for the first time since they are only accessible in the full radio-frequency interaction frame that requires a trimodal Floquet treatment. The comparison with numerical simulations shows that already small spin systems consisting of one S spin and two I spins describe the important features of the decoupling sequences quite realistically. The linewidth obtained from such numerical simulations of TPPM decoupling was 12 Hz. Taking into account the rf-field inhomogeneities and the strong dependence of the linewidth on the pulse length, this can explain the observed experimental linewidth in the order of 20–30 Hz, indicating that the achievable linewidths are at least partially limited by the presently available decoupling sequences.

ACKNOWLEDGMENTS

Financial support was provided by the Swiss National Science Foundation and the ETH Zürich through the TH system. We would like to thank Herbert Zimmermann from The MPI für Medizinische Forschung, Heidelberg for the preparation of the labeled glycine ethylester sample.

APPENDIX A: FOURIER COEFFICIENTS UNDER MAS

The Fourier coefficients of the Hamiltonian of Eq. (1) are defined in agreement with Ref. 1. The Fourier coefficients of the chemical-shift Hamiltonian are given by

$$\omega_{S_p}^{(n)} = \frac{2}{\sqrt{6}} \cdot d_{n,0}^2(\theta_r) \cdot e^{-in\gamma} \cdot \sum_{m=-2}^{2} d_{m,n}^2(\beta) \cdot e^{-im\alpha} \cdot \rho_{2,m}^{(S_p)} \tag{A1}$$

for $n \neq 0$ and

$$\omega_{S_p}^{(0)} = \omega_{S_p}^{\mathrm{iso}} \tag{A2}$$

for $n=0$. Here, $d_{m,n}^2(\beta)$ is the reduced Wigner matrix element; θ_r is the rotation angle; α, β, and γ are the three Euler angles which describe the orientation of the chemical-shift tensor in the rotor-fixed frame; and $\rho_{2,m}^{(S_p)}$ are the elements of the chemical-shift tensor in spherical-tensor notation. They are defined as

$$\rho_{2,0}^{(S_p)} = \sqrt{\frac{3}{2}}\delta_\sigma^{(S_p)},$$

$$\rho_{2,\pm 1}^{(S_p)} = 0, \tag{A3}$$

$$\rho_{2,\pm 2}^{(S_p)} = -\tfrac{1}{2}\delta_\sigma^{(S_p)}\eta_\sigma^{(S_p)}.$$

Here, the anisotropy of the chemical-shift tensor $\delta_\sigma^{(S_p)}$ is defined in angular frequency units and $\eta_\sigma^{(S_p)}$ is the asymmetry of the chemical-shift tensor.

The Fourier coefficients for the dipolar-coupling tensors are defined as

$$\begin{aligned}\omega_{I_\ell I_m}^{(n)} &= \frac{1}{\sqrt{6}} \cdot d_{n,0}^2(\theta_r) \cdot e^{-in\gamma} \cdot d_{0,n}^2(\beta) \cdot \rho_{2,0}^{(I_\ell I_m)} \\ &= \frac{1}{2\sqrt{3|n|}} |d_{0\cdot n}^2(\beta)| \cdot e^{-in\gamma} \cdot \delta_D^{(I_\ell I_m)} \\ &\quad \times (\text{for } \theta_r = \theta_m \approx 54.74^\circ),\end{aligned} \tag{A4}$$

with $n \neq 0$ where $d_{n,m}^2(\beta)$ is the reduced Wigner matrix element and the angles β and γ are the two Euler angles describing the orientation of the dipolar-coupling tensor in the rotor-fixed frame. The spherical-tensor elements are given by

$$\rho_{2,0}^{(I_\ell I_m)} = \sqrt{\frac{3}{2}}\delta_D^{(I_\ell I_m)}, \tag{A5}$$

and for $m \neq 0$

$$\rho_{2,m}^{(I_\ell I_m)} = 0. \tag{A6}$$

Here,

$$\delta_D^{(I_\ell I_m)} = -2 \cdot \frac{\mu_0}{4\pi} \cdot \frac{\gamma_I \gamma_I \hbar}{r_{I_\ell I_m}^3} \tag{A7}$$

is the anisotropy of the dipolar-coupling tensor in units of angular frequency. The second line of Eq. (A4) is only valid for $\theta_r = \theta_m \approx 54.74°$ (magic angle). For the heteronuclear dipolar-coupling tensor, analogous expressions hold true.

The Fourier coefficient of the homonuclear J couplings is defined as

$$\omega_{I_\ell I_m}^{(0)} = 2\pi J_{I_\ell I_m}, \tag{A8}$$

while the Fourier coefficient of the heteronuclear J coupling is defined as

$$\omega_{I_m S_p}^{(0)} = \pi J_{I_m S_p}. \tag{A9}$$

APPENDIX B: CALCULATION OF THE SECOND INTERACTION-FRAME FREQUENCY ω_α

In the following the third characteristic frequency ω_α of the TPPM Hamiltonian will be derived. Considering the basic building block of TPPM, consisting of two pulses with a flip angle β and phases $+\phi$ and $-\phi$, the interaction-frame representation is calculated analytically using a matrix representation. Only full cycles of TPPM irradiation are considered, i.e., all side bands at multiples of ω_m are folded back onto the center band. The rf part of the Hamiltonian during the two pulses is given by

$$\begin{aligned}\mathcal{H}_\phi(t) &= \omega_1(I_{\ell z}\cos(\varphi(t)) + I_{\ell y}\sin(\varphi(t))), \\ \mathcal{H}_{-\phi}(t) &= \omega_1(I_{\ell z}\cos((\varphi(t)) - I_{\ell y}\sin(\varphi(t))))\end{aligned} \tag{B1}$$

leading to the propagators

$$\begin{aligned}U_\phi(\beta) &= \exp(-i\mathcal{H}_\phi\tau_p), \\ U_{-\phi}(\beta) &= \exp(-i\mathcal{H}_{-\phi}\tau_p),\end{aligned} \tag{B2}$$

where $\beta = \omega_1\tau_p$. The full propagator for the interaction-frame transformation of the TPPM irradiation scheme after n full cycles is given by

$$U(n) = (U_\phi U_{-\phi})^n. \tag{B3}$$

The matrix representation of this propagator can be calculated analytically and the interaction-frame expressions for the spin operators contain only terms of the form

$$\begin{aligned}&\left[\cos\beta\cos^2\phi \right. \\ &\left. + \sin^2\phi \pm i\sqrt{\cos^2\phi\sin^2\beta + \sin^4\frac{\beta}{4}\sin^2(2\phi)}\right]^n \\ &= e^{\pm in\alpha} = e^{\pm i\omega_\alpha t},\end{aligned} \tag{B4}$$

which depend on n with

$$\alpha = \arccos(\cos\beta\cos^2\phi + \sin^2\phi). \tag{B5}$$

The frequency ω_α agrees with values obtained from numerical interaction-frame calculations of the TPPM sequence. The frequency corresponds to the magnitude of the effective nutation about an axis that describes the combined rotation of the two pulses in a TPPM cycle.

APPENDIX C: DEFINITION OF CONSTANTS

The $q_{x\mu}^{(\nu)}$ of Eq. (19) are a shorthand notation for $q_{x\mu}^{(\nu,0,0)}$. The more general constants $q_{x\mu}^{(\nu,k_0,\ell_0)}$ are defined as

$$q_{xx}^{(\nu,k_0,\ell_0)} = \sum_{\kappa=-\infty}^{\infty} \sum_{\lambda=-1}^{1} \frac{a_{xz}^{(k_0-\kappa,\ell_0-\lambda)} a_{xy}^{(\kappa,\lambda)} - a_{xy}^{(k_0-\kappa,\ell_0-\lambda)} a_{xz}^{(\kappa,\lambda)}}{\nu\omega_r + \kappa\omega_m + \lambda\omega_\alpha}, \tag{C1}$$

$$q_{xy}^{(\nu,k_0,\ell_0)} = \sum_{\kappa=-\infty}^{\infty} \sum_{\lambda=-1}^{1} \frac{a_{xx}^{(k_0-\kappa,\ell_0-\lambda)} a_{xz}^{(\kappa,\lambda)} - a_{xz}^{(k_0-\kappa,\ell_0-\lambda)} a_{xz}^{(\kappa,\lambda)}}{\nu\omega_r + \kappa\omega_m + \lambda\omega_\alpha}, \tag{C2}$$

and

$$q_{xz}^{(\nu,k_0,\ell_0)} = \sum_{\kappa=-\infty}^{\infty} \sum_{\lambda=-1}^{1} \frac{a_{xy}^{(k_0-\kappa,\ell_0-\lambda)} a_{xx}^{(\kappa,\lambda)} - a_{xx}^{(k_0-\kappa,\ell_0-\lambda)} a_{xy}^{(\kappa,\lambda)}}{\nu\omega_r + \kappa\omega_m + \lambda\omega_\alpha}. \tag{C3}$$

The parameters $q_{z\mu\chi}^{(\nu)}$ and $\tilde{q}_{z\mu\chi}^{(\nu)}$ of Eq. (20) are given by

$$q_{z\mu x}^{(\nu)} = \sum_{\kappa=-\infty}^{\infty} \sum_{\lambda=-2}^{2} \frac{a_{xz}^{(\mp\kappa,\mp\lambda)} a_{xx,\mu y}^{(\pm\kappa,\pm\lambda)} - a_{xy}^{(\mp\kappa,\mp\lambda)} a_{xx,\mu z}^{(\pm\kappa,\pm\lambda)}}{\nu\omega_r + \kappa\omega_m + \lambda\omega_\alpha}, \tag{C4}$$

$$q_{z\mu y}^{(\nu)} = \sum_{\kappa=-\infty}^{\infty} \sum_{\lambda=-2}^{2} \frac{a_{xx}^{(\mp\kappa,\mp\lambda)} a_{xx,\mu z}^{(\pm\kappa,\pm\lambda)} - a_{xz}^{(\mp\kappa,\mp\lambda)} a_{xx,\mu x}^{(\pm\kappa,\pm\lambda)}}{\nu\omega_r + \kappa\omega_m + \lambda\omega_\alpha}, \tag{C5}$$

$$q_{z\mu z}^{(\nu)} = \sum_{\kappa=-\infty}^{\infty} \sum_{\lambda=-2}^{2} \frac{a_{xy}^{(\mp\kappa,\mp\lambda)} a_{xx,\mu x}^{(\pm\kappa,\pm\lambda)} - a_{xx}^{(\mp\kappa,\mp\lambda)} a_{xx,\mu y}^{(\pm\kappa,\pm\lambda)}}{\nu\omega_r + \kappa\omega_m + \lambda\omega_\alpha}, \tag{C6}$$

and

$$\tilde{q}_{zx\chi}^{(\nu)} = \sum_{\kappa=-\infty}^{\infty} \sum_{\lambda=-2}^{2} \frac{a_{xz}^{(\mp\kappa,\mp\lambda)} a_{xx,y\chi}^{(\pm\kappa,\pm\lambda)} - a_{xy}^{(\mp\kappa,\mp\lambda)} a_{xx,z\chi}^{(\pm\kappa,\pm\lambda)}}{\nu\omega_r + \kappa\omega_m + \lambda\omega_\alpha}, \tag{C7}$$

$$\tilde{q}_{zy\chi}^{(\nu)} = \sum_{\kappa=-\infty}^{\infty} \sum_{\lambda=-2}^{2} \frac{a_{xx}^{(\mp\kappa,\mp\lambda)} a_{xx,z\chi}^{(\pm\kappa,\pm\lambda)} - a_{xz}^{(\mp\kappa,\mp\lambda)} a_{xx,x\chi}^{(\pm\kappa,\pm\lambda)}}{\nu\omega_r + \kappa\omega_m + \lambda\omega_\alpha}, \tag{C8}$$

$$\tilde{q}_{zz\chi}^{(\nu)} = \sum_{\kappa=-\infty}^{\infty} \sum_{\lambda=-2}^{2} \frac{a_{xy}^{(\mp\kappa,\mp\lambda)} a_{xx,x\chi}^{(\pm\kappa,\pm\lambda)} - a_{xx}^{(\mp\kappa,\mp\lambda)} a_{xx,y\chi}^{(\pm\kappa,\pm\lambda)}}{\nu\omega_r + \kappa\omega_m + \lambda\omega_\alpha}. \tag{C9}$$

The constants $p_{\mu\chi\xi}^{(\nu)}$ of Eq. (21) are then given by

$$p_{\mu x\xi}^{(\mp\nu)} = \sum_{\kappa=-\infty}^{\infty} \sum_{\lambda=-2}^{2} \frac{a_{xx,\mu z}^{(\mp\kappa,\mp\lambda)} a_{xx,y\xi}^{(\pm\kappa,\pm\lambda)} - a_{xx,\mu y}^{(\mp\kappa,\mp\lambda)} a_{xx,z\xi}^{(\pm\kappa,\pm\lambda)}}{\nu\omega_r + \kappa\omega_m + \lambda\omega_\alpha}, \tag{C10}$$

$$p_{\mu y\xi}^{(\mp\nu)} = \sum_{\kappa=-\infty}^{\infty} \sum_{\lambda=-2}^{2} \frac{a_{xx,\mu x}^{(\mp\kappa,\mp\lambda)} a_{xx,z\xi}^{(\pm\kappa,\pm\lambda)} - a_{xx,\mu z}^{(\mp\kappa,\mp\lambda)} a_{xx,x\xi}^{(\pm\kappa,\pm\lambda)}}{\nu\omega_r + \kappa\omega_m + \lambda\omega_\alpha}, \tag{C11}$$

and

$$p_{\mu z\xi}^{(\mp\nu)} = \sum_{\kappa=-\infty}^{\infty} \sum_{\lambda=-2}^{2} \frac{a_{xx,\mu y}^{(\mp\kappa,\mp\lambda)} a_{xx,x\xi}^{(\pm\kappa,\pm\lambda)} - a_{xx,\mu x}^{(\mp\kappa,\mp\lambda)} a_{xx,y\xi}^{(\pm\kappa,\pm\lambda)}}{\nu\omega_r + \kappa\omega_m + \lambda\omega_\alpha}. \tag{C12}$$

Here the indices μ and ξ have to be permuted through all possible orientations independently.

The constants $p_{\mu}^{(\nu)}$ of Eq. (21) are given by

$$p_{x}^{(\nu)} = \sum_{\chi} \sum_{\kappa=-\infty}^{\infty} \sum_{\lambda=-2}^{2} \frac{a_{xx,z\chi}^{(\mp\kappa,\mp\lambda)} a_{xx,y\chi}^{(\pm\kappa,\pm\lambda)} - a_{xx,y\chi}^{(\mp\kappa,\mp\lambda)} a_{xx,z\chi}^{(\pm\kappa,\pm\lambda)}}{\nu\omega_r + \kappa\omega_m + \lambda\omega_\alpha}, \tag{C13}$$

$$p_{y}^{(\nu)} = \sum_{\chi} \sum_{\kappa=-\infty}^{\infty} \sum_{\lambda=-2}^{2} \frac{a_{xx,x\chi}^{(\mp\kappa,\mp\lambda)} a_{xx,z\chi}^{(\pm\kappa,\pm\lambda)} - a_{xx,z\chi}^{(\mp\kappa,\mp\lambda)} a_{xx,x\chi}^{(\pm\kappa,\pm\lambda)}}{\nu\omega_r + \kappa\omega_m + \lambda\omega_\alpha}, \tag{C14}$$

and

$$p_{z}^{(\nu)} = \sum_{\chi} \sum_{\kappa=-\infty}^{\infty} \sum_{\lambda=-2}^{2} \frac{a_{xx,y\chi}^{(\mp\kappa,\mp\lambda)} a_{xx,x\chi}^{(\pm\kappa,\pm\lambda)} - a_{xx,x\chi}^{(\mp\kappa,\mp\lambda)} a_{xx,y\chi}^{(\pm\kappa,\pm\lambda)}}{\nu\omega_r + \kappa\omega_m + \lambda\omega_\alpha}. \tag{C15}$$

[1] M. Ernst, J. Magn. Reson. **162**, 1 (2003).
[2] P. Hodgkinson, Prog. Nucl. Magn. Reson. Spectrosc. **46**, 197 (2005).
[3] M. Mehring, *Principles of High Resolution NMR in Solids*, 2nd ed. (Springer, Berlin, 1983).
[4] I. J. Shannon, K. D. M. Harris, and S. Arumugan, Chem. Phys. Lett. **196**, 588 (1992).
[5] M. Ernst, H. Zimmermann, and B. H. Meier, Chem. Phys. Lett. **317**, 581 (2000).
[6] G. Sinning, M. Mehring, and A. Pines, Chem. Phys. Lett. **43**, 382 (1976).
[7] M. Mehring and G. Sinning, Phys. Rev. B **15**, 2519 (1977).
[8] A. E. Bennett, C. M. Rienstra, M. Auger, K. V. Lakshmi, and R. G. Griffin, J. Chem. Phys. **103**, 6951 (1995).
[9] Z. H. Gan and R. R. Ernst, Solid State Nucl. Magn. Reson. **8**, 153 (1997).
[10] Y. L. Yu and B. M. Fung, J. Magn. Reson. **130**, 317 (1998).
[11] B. M. Fung, A. K. Khitrin, and K. Ermolaev, J. Magn. Reson. **142**, 97 (2000).
[12] A. Khitrin and B. M. Fung, J. Chem. Phys. **112**, 2392 (2000).
[13] K. Takegoshi, J. Mizokami, and T. Terao, Chem. Phys. Lett. **341**, 540 (2001).
[14] G. Gerbaud, F. Ziarelli, and S. Caldarelli, Chem. Phys. Lett. **377**, 1 (2003).
[15] G. De Paëpe, B. Elena, and L. Emsley, J. Chem. Phys. **121**, 3165 (2004).
[16] R. S. Thakur, N. D. Kurur, and P. K. Madhu, Chem. Phys. Lett. **426**, 459 (2006).
[17] G. De Paëpe, P. Hodgkinson, and L. Emsley, Chem. Phys. Lett. **376**, 259 (2003).
[18] M. Edén and M. H. Levitt, J. Chem. Phys. **111**, 1511 (1999).
[19] J. Leppert, O. Ohlenschläger, M. Görlach, and R. Ramachandran, J. Biomol. NMR **29**, 319 (2004).
[20] G. De Paëpe, A. Lesage, and L. Emsley, J. Chem. Phys. **119**, 4833 (2003).
[21] G. De Paëpe, D. Sakellariou, P. Hodgkinson, S. Hediger, and L. Emsley, Chem. Phys. Lett. **368**, 511 (2003).
[22] P. Tekely, P. Palmas, and D. Canet, J. Magn. Reson., Ser. A **107**, 129 (1994).
[23] A. Detken, E. H. Hardy, M. Ernst, and B. H. Meier, Chem. Phys. Lett. **356**, 298 (2002).
[24] M. Ernst, A. Samoson, and B. H. Meier, Chem. Phys. Lett. **348**, 293 (2001).
[25] M. Ernst, A. Samoson, and B. H. Meier, J. Magn. Reson. **163**, 332 (2003).
[26] M. Ernst, M. A. Meier, T. Tuherm, A. Samoson, and B. H. Meier, J. Am. Chem. Soc. **126**, 4764 (2004).

[27] M. Kotecha, N. P. Wickramasinghe, and Y. Ishii, Magn. Reson. Chem. **45**, S221 (2007).
[28] X. Filip, C. Tripon, and C. Filip, J. Magn. Reson. **176**, 239 (2005).
[29] G. De Paëpe, N. Giraud, A. Lesage, P. Hodgkinson, A. Böckmann, and L. Emsley, J. Am. Chem. Soc. **125**, 13938 (2003).
[30] U. Haeberlen, *High Resolution NMR in Solids: Selective Averaging* (Academic, New York, 1976).
[31] M. Ernst, S. Bush, A. C. Kolbert, and A. Pines, J. Chem. Phys. **105**, 3387 (1996).
[32] A. Khitrin, T. Fujiwara, and H. Akutsu, J. Magn. Reson. **162**, 46 (2003).
[33] M. Carravetta, M. Edén, X. Zhao, A. Brinkmann, and M. H. Levitt, Chem. Phys. Lett. **321**, 205 (2000).
[34] M. Baldus, T. O. Levante, and B. H. Meier, Z. Naturforsch., A: Phys. Sci. **49a**, 80 (1994).
[35] E. Vinogradov, P. K. Madhu, and S. Vega, Chem. Phys. Lett. **329**, 207 (2000).
[36] E. Vinogradov, P. K. Madhu, and S. Vega, J. Chem. Phys. **115**, 8983 (2001).
[37] R. Ramesh and M. S. Krishnan, J. Chem. Phys. **114**, 5967 (2001).
[38] M. Ernst, A. Samoson, and B. H. Meier, J. Phys. Chem. **123**, 064102 (2005).
[39] J. R. Sachleben, J. Gaba, and L. Emsley, Solid State Nucl. Magn. Reson. **29**, 30 (2006).
[40] R. Ramachandran, V. S. Bajaj, and R. G. Griffin, J. Chem. Phys. **122**, 164503 (2005).
[41] M. Ernst, H. Geen, and B. H. Meier, Solid State Nucl. Magn. Reson. **29**, 2 (2006).
[42] M. Leskes, R. S. Thakur, P. K. Madhu, N. D. Kurur, and S. Vega, J. Chem. Phys. **127**, 024501 (2007).
[43] I. Scholz, B. H. Meier, and M. Ernst, J. Chem. Phys. **127**, 204504 (2007).
[44] P. Hodgkinson, PNMRSIM, a general simulation program for large problems in solid-state NMR. Available from: http://www.durham.ac.uk/paul.hodgkinson/pNMRsim/ (2008).
[45] V. E. Zorin, M. Ernst, S. P. Brown, and P. Hodgkinson, J. Magn. Reson. **192**, 183 (2008).
[46] H. J. Reich, M. Jautelat, M. T. Messe, F. J. Weigert, and J. D. Roberts, J. Am. Chem. Soc. **91**, 7445 (1969).
[47] B. Birdsall, N. J. M. Birdsall, and J. Feeney, J. Chem. Soc., Chem. Commun. **1972**, 316 (1972).
[48] G. De Paëpe, M. J. Bayro, J. Lewandowski, and R. G. Griffin, J. Am. Chem. Soc. **128**, 1776 (2006).